Molar Element Ratio Analysis of Lithogeochemical Data: A Toolbox for Use in Mineral Exploration and Mining

Stanley, C. [1]

_____

1. Dept. of Earth & Environmental Science, Acadia University, Wolfville, N.S., Canada, B4P 2R6

ABSTRACT

Over the last half century, lithogeochemical data analysis has evolved substantially, and a number of useful quantitative tools are now available to the explorationist to facilitate a variety of exploration tasks. Today, many mining companies are using lithogeochemistry as a validator to assist explorationists in regional-to-property scale mapping, and drill-core logging. However, lithogeochemical data are also capable of being used to classify rocks, and assist in a number of other tactical and strategic exploration activities, including: correlation of stratigraphy on cross-sections, development of mineral zoning models in plan and section, determination of host rock geochemical affinity and depositional environment, understanding the genesis of both host rocks and mineral deposits, and identification of precipitation mechanisms for mineralization. Clearly, lithogeochemical data analysis is now making substantial contributions to mineral exploration efforts.

Molar element ratio analysis is one of the principal methods used by explorationists today to evaluate lithogeochemical data. This approach is one of several that avoid the effects of closure, the constraint that element concentrations sum to unity. Unfortunately, closure adds mathematically induced variance to lithogeochemical data that obscures the effects of rock-forming and rock-altering processes. However, two distinctive advantages of molar element ratio analysis, relative to other material transfer techniques that also avoid closure, are that: it examines data in a molar context, allowing investigation of rock compositions in terms of the minerals comprising the rocks and the chemical reactions that alter the rocks, and it can consider more than two samples at a time, allowing rapid investigation of large lithogeochemical datasets.

Molar element ratio analysis consists of four basic tools that provide substantial insight into the lithogeochemistry (and mineralogy) of the rocks under investigation. These tools consist of: (i) conserved element analysis, (ii) Pearce element ratio analysis, (iii) general element ratio analysis, and (iv) change of basis rock classification. Conserved element analysis is useful in creating a chemostratigraphic model for the host rocks to mineral deposits, whereas Pearce and general element ratio analysis have primarily been used to identify the major mineralogical and metasomatic controls on rock compositions, and to investigate and quantify the extent of material transfer processes that formed the host rocks and mineralization. Change of basis rock classification converts element concentrations into mineral concentrations, allowing lithogeochemical data to be interpreted in terms of minerals and used to provide proper names to rocks, an important activity because of the implications that rock names have on genetic processes and mineral deposit models.

This paper provides a review of the theoretical foundations of each of these four tools, and then illustrates how these techniques have been used in a variety of exploration applications to assist in the exploration for, evaluation and planning of, and the mining of mineral deposits. Examples include the evaluation of lithogeochemical datasets from mineral deposits hosted by igneous and sedimentary rocks and formed by hydrothermal and igneous processes. In addition, this paper illustrates a more recent geometallurgical application of these methods, whereby the mineral proportions determined by the change of basis rock classification are used to predict rock properties and obtain the ore body knowledge critical to resource evaluation, mine planning, mining, and mine remediation.

INTRODUCTION

Since the development of analytical procedures capable of rapidly, inexpensively, and accurately producing multi-element whole rock major oxide concentration estimates, largely due to the development of commercial energy-dispersive x-ray fluorescence spectrometers in the 1950s (Jenkins, 2012), lithogeochemical data have been evaluated by the mining industry in a variety of ways. Historically, most lithogeochemical data analysis was undertaken in support of mineral exploration applications (e.g., hydrothermal alteration assemblage mapping). More recently, these lithogeochemical data analysis applications have expanded into the field of geometallurgy, for use in mineral deposit resource assessment,

mine planning, mining, and mine remediation.

Early on, most data analysis procedures were relatively simple and univariate in nature. However, the broader array of mining industry applications and availability of multi-element analytical procedures has necessitated employing more sophisticated lithogeochemical data evaluation methods that avoid interferences caused by 'closure', the constraint, that compositions of components of a whole sum to unity (Aitchison, 1986). Closure imposes additional compositional variability that obscures real geological variations in rocks, and thus significantly influences both data evaluation method selection and data interpretation.

A principal data analysis procedure gaining favour today is molar element ratio analysis (MER; Stanley and Madeisky, 1996; Stanley, 1998), a set of procedures that evaluate major oxide concentrations in terms of the minerals in the rocks, while also avoiding the effects of closure. These procedures are now in common use, not only because of the technical knowledge that they have been able to offer the mineral explorationist, but because of the facility with which these procedures can be undertaken using modern software packages with embedded MER analysis calculations and diagrams (e.g., ioGas®, R®).

The MER lithogeochemistry data evaluation strategy employs four tools to gain insight into the nature and controls on rock compositions: (i) conserved element analysis, (ii) Pearce element ratio analysis, (iii) general element ratio analysis, and (iv) change of basis rock classification.

Conserved element analysis is an exploratory data evaluation approach that involves the examination of scatterplots and other diagrams comprised of elements that are 'conserved' (do not undergo material transfer during processes that change the composition; Nicholls, 1988, Russell and Stanley, 1990) in the rocks under examination. The relationships between conserved element concentrations allow discrimination of rock suites with different starting compositions, and so facilitate stratigraphic correlation. In addition, conserved element ratios are commonly used to establish the geochemical affinity and tectonic environment of the host rocks (e.g., Pearce, 1996), and comprise the standardizing denominators of Pearce element ratios.

Pearce element ratio (PER) analysis is a hypothesis-testing paradigm for the evaluation of rock geochemistry, and generally provides an understanding of the nature and extent of material transfer that has taken place in a suite of rocks. Developed by Thomas H. Pearce (1968), these ratios are proportional to the magnitude of material transfer in rocks if a conserved element is used in their denominator. Diagrams comprised of PERs facilitate the investigation of material transfers responsible for compositional diversity in rocks, as these displace rock compositions along lines with slopes corresponding to the stoichiometry of the material transfers. Consequently, PER analysis provides insight into the processes responsible for rock genesis, and quantifies the extent to which these processes have occurred in rocks.

Stanley (1998) developed general element ratio (GER) analysis as a complementary hypothesis-testing data analysis method to Pearce element ratio analysis. It differs from PER analysis in that the denominator element in GERs is not conserved, but rather fully participates in material transfer. As a result, material transfer behaves differently on GER diagrams than on PER diagrams, as the material transfers plot at nodes (or anti-nodes) on the GER diagrams. Rocks affected by these material transfers have compositions that are displaced toward (or away from) the nodes (anti-nodes), and thus are equally interpretable and quantifiable.

Collectively, PER and GER diagrams can be used to investigate material transfer in any rock suite, precisely because the suite either contains a conserved element, or it doesn't. Consequently, these two data analysis tools can be used to understand the nature and magnitude of material transfer in any suite of rocks, and so have been effective in mineral exploration by vectoring, for example, into the cores of hydrothermal systems responsible for the formation of mineral deposits (Madeisky and Stanley, 1993; Robinson et al., 1996; Mireku and Stanley, 2007; O'Connor-Parsons and Stanley, 2007; Murphy and Stanley, 2007; Benavides et al., 2008a, 2008b; Urqueta et al., 2009; Polito et al., 2009, 2011).

Lastly, the 'change of basis' rock classification procedure was recently developed by Stanley (2017). This is effectively a data transformation tool that converts lithogeochemical data into the modal mineralogical data with which geologists classify and investigate rocks. This procedure employs linear algebra to convert rock compositions described in terms of element concentrations into rock compositions described in terms of mineral concentrations. These mineral concentrations can then be plotted on a variety of ternary diagrams used in classification (Streckeisen et al., 2002), or used to create mineralogical zoning models across mineral deposits. More recent applications of this procedure involve using the mineral concentrations to estimate bulk rock properties during mining feasibility studies of mineral deposits.

In the descriptions of these four data analysis tools below, examples of the MER diagrams used to evaluate lithogeochemical data are presented, along with brief mathematical proofs to illustrate the theoretical foundation on which these methods are based.

CONSERVED ELEMENT ANALYSIS

Conserved element analysis is typically undertaken first when evaluating lithogeochemical data using molar element ratios. Its purpose is to identify the natural groupings in the data that reflect individual lithologies, and thus assists in stratigraphic correlation. Conserved element analysis is founded on the principle that ratios of conserved elements do not change during material transfer (Vistelius and Sarmanov, 1961). This principle can be validated by considering the formula defining the concentration of an element (z; in mass percent):

$$z = \frac{Z}{S}, \qquad \text{(E1)}$$

where Z is the amount of the conserved element in the rock (in grams), and S is the mass of the rock (in grams). If we form a ratio of two conserved element concentrations (z_a & z_b), we have:

$$\frac{z_a}{z_b} = \frac{Z_a/S}{Z_b/S} = \frac{Z_a}{Z_b}. \qquad \text{(E2)}$$

Now, if a suite of rocks, initially of constant composition, are variably affected by a material transfer process that adds or removes other elements (say Y) to or from the rocks, the rock masses (S) will change ($dS \neq 0$), but the masses of the conserved elements (Z_a, Z_b) in all of these rocks, because they are conserved, will not ($dZ_a = dZ_b = 0$). Consequently, the ratios of conserved element masses (Z_a/Z_b) in all of the rocks will be constant, as will the ratio of the conserved element concentrations (z_a/z_b; by Equation E2), even though the actual

concentrations may change substantially. This conserved element concentration ratio is effectively a constant parameter common to the entire rock suite, and can be used to identify rocks of common (cogenetic) parentage during stratigraphic correlation.

Element concentrations are commonly plotted on a number of different diagrams in order to identify conserved elements and cogenetic rocks (*i.e.*, test the cogenetic hypothesis; Russell and Stanley, 1990). The concentrations of conserved element concentrations manifest themselves differently on each diagram. For example, when two conserved elements are plotted against each other on a scatterplot (e.g., Shervais, 1982), samples exhibiting a common conserved element ratio plot on a line, given measurement error, that passes through the origin and has a slope equal to the ratio (Figure 1).
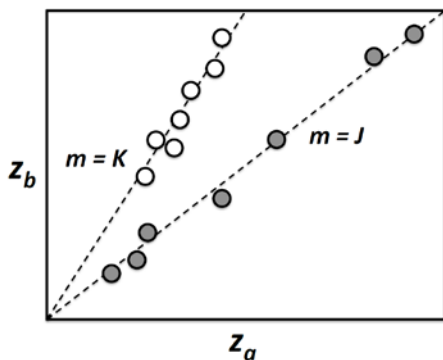
Figure 1: Schematic scatterplot of two conserved element concentrations (z_a & z_b), illustrating two different suites of cogenetic rocks (grey and white circles) that plot on lines with different slopes (J & K) through the origin.

When plotted on a ternary diagram (e.g., Meschede, 1986), the three conserved elements must be first standardized to sum to unity (Figure 2). On these diagrams, conserved elements plot at a single point defined by two ratios of the three conserved elements (z_b/z_a & z_c/z_a).
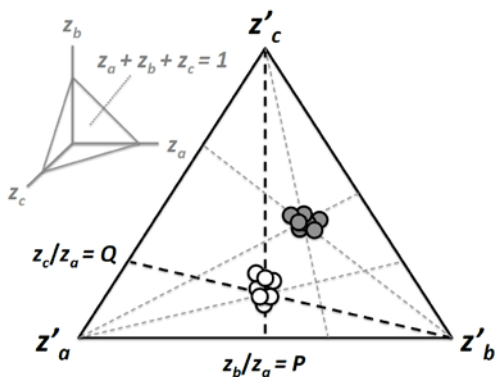

Figure 2: Schematic ternary diagram comprised of three conserved elements (z_a, z_b, & z_c), defined by different z_b/z_a and z_c/z_a ratios [note that the third ratio, $z_c/z_b = z_c/z_a / z_b/z_a$] illustrating two different suites of cogenetic rocks.

When four conserved elements are plotted on a log-ratio scatterplot (e.g., Winchester and Floyd, 1977), the conserved elements also plot at a single point defined by two ratios with different denominators (Figure 3).
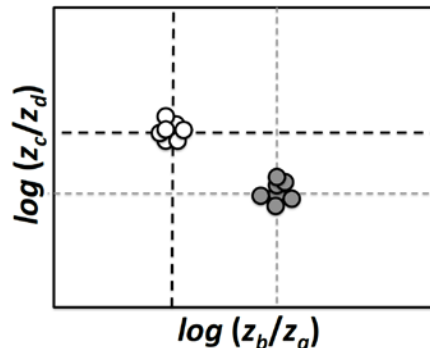

Figure 3: Schematic log-ratio diagram comprised of four conserved elements (z_a, z_b, z_c, & z_d) and plotting *log* z_b/z_a against *log* z_c/z_d illustrating two different suites of cogenetic rocks.

Finally, it is worth noting that logarithmically scaled spidergrams (e.g., Sun and McDonough, 1989; Figure 4) are commonly used to discriminate between rock suites, and are also founded on conserved element principles. This is because the slopes of lines linking two standardized element concentrations on logarithmically scaled spidergrams are proportional to the standardized ratio of those element concentrations. Thus, lines between element pairs that have common slopes on such spidergrams are also a criterion for element conservation. Interpreted in this way, two samples with the same conserved element concentration patterns (inter-element slopes) on a logarithmically scaled spidergram are cogenetic, as these element concentrations have either been diluted or enriched proportionally by a material transfer process that doesn't involve the elements on the spidergram. Thus, logarithmically-scaled spidergrams can be very powerful tests of the cogenetic hypothesis, because they allow for the simultaneous comparison of a very large number of conserved element ratios (*n×(n-1))*, if the spidergram is composed of *n* elements), at least provided that the number of samples is small so that the patterns are discernable via visual analysis.
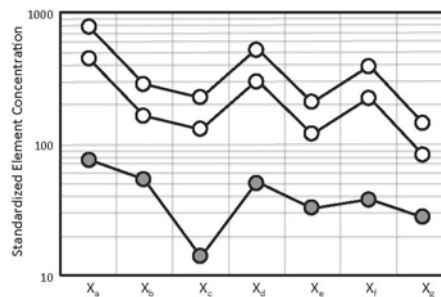

Figure 4: Schematic spidergram illustrating conserved element concentrations with equal ratios/parallel patterns (orange) and different ratios/different patterns (blue).

Several other types of hybrid conserved element diagrams (e.g., Zr/TiO_2 versus SiO_2; Kramar, 2017) have also been used in lithogeochemical data analysis, but all involve at least one variable whose behavior is founded on the principle that the conserved element ratios in cogenetic rocks are constant.

PEARCE ELEMENT RATIO ANALYSIS

Pearce element ratio analysis (Pearce, 1968) can only be undertaken after conserved element analysis, because a conserved element must be identified for the denominator before PERs can be constructed. Philosophically, PERs have a molar format so that variations in rock compositions can be understood in terms of material transfers that occur as minerals (e.g., fractional crystallization) or elements (e.g., metasomatic reactions).

The conserved element in a PER serves as a standardizing variable to avoid the effects of 'closure', a mathematical effect that obscures the true variations in a rock suite caused by material transfer. Closure is caused by the constraint that rock compositions sum to unity. The conserved element causes variations in the PER to be proportional to material transfers among the numerator element. For example, taking the derivative of a PER (*x/z*; from Equation E2) yields:

$$d\left(\frac{x}{z}\right) = d\left(\frac{X}{Z}\right) = \frac{dX}{Z} - \frac{XdZ}{Z^2} = \frac{ZdX - XdZ}{Z^2}. \quad \text{(E3)}$$

However, because the denominator element *Z* is conserved (is neither added nor removed during material transfer), $dZ = 0$, so Equation E3 becomes:

$$d\left(\frac{x}{z}\right) = \frac{ZdX}{Z^2} = \frac{dX}{Z}. \quad \text{(E4)}$$

Consequently, changes to a PER (*d(x/z)*) are proportional to changes to the numerator element (*dX*) during material transfer, and *Z* is the proportionality constant. Thus, when two PERs (*x/z, y/z*) are plotted against each other on a scatterplot, they reveal, via the slope of the data trend (Equation E5), the stoichiometry of the material transfer process (*dY/dX*) that caused the compositions in rock suite to change (Figure 5):

$$m = d\left(\frac{d(y/z)}{d(x/z)}\right) = \frac{(dY/Z)}{(dX/Z)} = \frac{dY}{dX}. \quad \text{(E5)}$$

Linear combinations of PERs (e.g., *(Ax_a+Bx_b)/z*) plotted against each other change the location in geochemical space from which the rock compositions are examined. These linear combinations can be derived using matrix algebra procedures (Stanley and Russell, 1989; Nicholls and Gordon, 1994), allowing complicated material transfer processes to be projected from (e.g., the fractional crystallization of three minerals in a mafic intrusion, such as olivine, plagioclase and clinopyroxene) to isolate the material transfer process of interest (e.g., hydrothermal alteration that subsequently affected the intrusion, such as the muscovite alteration of plagioclase). This endows such PER diagrams with substantial investigative power, allowing recognition of the processes responsible for rock

formation. Furthermore, because of the proportionality between PERs and material transfer, quantitative estimates of the magnitude of these rock-forming processes can be obtained, allowing the explorationist, for example, to create maps of hydrothermal alteration intensity.
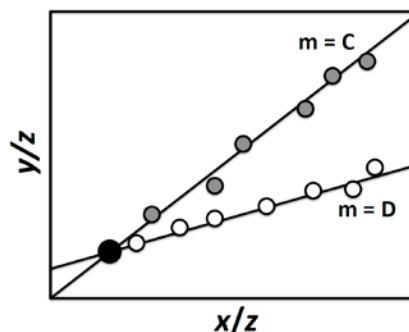

Figure 5: Schematic PER diagram illustrating the effects of two material transfer processes with different stoichiometries (dy/dx = C: grey and dy/dx = D: white) affecting a suite of cogenetic rocks with a common parent composition (black).

In practice, simple PERs are calculated by first dividing mass-based element concentrations (from geochemical laboratories) by their corresponding gram formula weights, and then forming ratios of these quotients, ensuring that the denominator element is conserved. Linear combinations of these simple PERs then produce more complicated PERs that project from specific material transfer processes (e.g., $A(x_a/z)+B(x_b/z) = (Ax_a+Bx_b)/z$). If more than one conserved element is available (analyzed and confirmed as conserved using diagrams of the ilk presented in Figures 1-3), then the conserved element used should be the one with the lowest relative measurement error, as this will endow the PERs formed from it with the highest resolution.

GENERAL ELEMENT RATIO ANALYSIS

General element ratios (GERs) are similar to PERs in that they also have a molar format (Stanley and Madeisky, 1996; Stanley, 1998). However, instead of having a conserved element denominator that is neither added nor removed, their denominator participates in the material transfer process that caused the compositions in a rock suite to vary. This makes the material transfer behavior of a GER diagram different from that of a PER diagram, but no less interpretable.

Because the denominator element is not conserved, changes to a GER are described by Equation E3 instead of Equation E4. Thus, when two GERs (*x/z, y/z*) are plotted on a scatterplot, they reveal, via the slope of the data trend, both the stoichiometry of the material transfer process (*dX/dZ* & *dY/dZ*) that caused the compositions in a rock suite to change, and the initial rock composition (*y/z* & *x/z*):

$$m = \frac{dY/Z - ydZ/Z}{dX/Z - xdZ/Z} = \frac{dY - ydZ}{dX - xdZ} = \frac{dY/dZ - y/z}{dX/dZ - x/z}. \quad \text{(E6)}$$

The data trend is thus a line between two points: (*x/z, y/z*) and (*dX/dZ, dY/dZ*), both of which plot on GER diagrams (Figure 6).

Consequently, material transfers (whether they occur as minerals or element combinations as part of a metasomatic reaction) plot as points on GER diagrams (in contrast to the effects of material transfer on PER diagrams), causing material transfer to move rock compositions toward or away from these points as it proceeds. Thus, the extent of material transfer on GER diagrams is just as measureable as on PER diagrams, except that the lever rule applies (Smith and Hashemi, 2006).

Again, linear combinations of GERs can also be constructed and plotted against each other to test complicated material transfer processes. These linear combinations can be derived using the same matrix algebra procedures as those employed for PERs (Stanley and Russell, 1989; Nicholls and Gordon, 1994). This makes GER diagrams extremely powerful means to test petrologic or metasomatic processes, and consequently serves as a very useful tool in lithogeochemical data analysis.
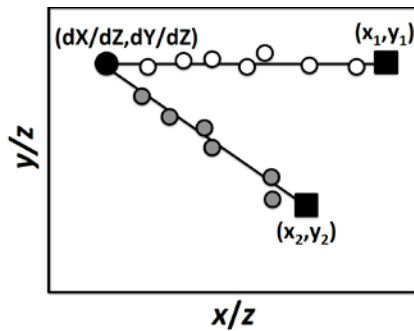

Figure 6: Schematic GER diagram illustrating that as a material transfer process proceeds, two different rock compositions move from their starting compositions (x, y) toward or away from the composition defined by the material transfer stoichiometry (dX/dZ, dY/dZ).

On both PER and GER diagrams, sets of two hypotheses are tested simultaneously during data analysis. PER diagrams test whether the denominator element is conserved ($dZ = 0$) and whether the data plot on the diagram along lines with slopes consistent with a specific material transfer ($dY/dX = p$). In contrast, GER diagrams test whether the data plot on the diagram along lines that pass through intercepts consistent with the material transfer process ($dX/dZ = q$ and $dY/dZ = r$). In both cases, there are two equations (hypotheses) involving three potential material transfers (dX, dY, dZ). This common feature, along with many additional complementary characteristics, make these two forms of MER analysis analogous, compatible, and when used in tandem, highly synergistic lithogeochemical investigation tools.

CHANGE OF BASIS ROCK CLASSIFICATION

Change of basis rock classification is the fourth tool in the MER lithogeochemical toolbox (Stanley, 2017), but it differs from the other procedures, because it is not really a data analysis tool. Rather, it is merely a transformation procedure that converts the conventional way we describe rock compositions (as element concentrations) into mineral concentrations. Consequently, this

procedure allows the geologist to investigate rock compositions in terms of the building blocks of rocks (minerals), and provides an alternative way of examining how rock compositions vary (in terms of mineral concentrations, instead of element concentrations).

The change of basis rock classification procedure (Stanley, 2017) involves several calculations to convert element concentrations into mineral concentrations. These steps are illustrated in Figure 7. The first step involves identification of the 'essential' mineral assemblage that will be used to describe the rock compositions. These essential minerals are the major and minor minerals in the rocks, and are defined as those minerals that occur in concentrations greater than 5% in at least 5% of the rocks. Once identified, the elements that have been analyzed and occur within these n essential minerals are identified and placed in a matrix (C), with the essential minerals along the side, and the moles of each element in these minerals along the top (Equation E7). Note that the number of elements (n) must equal the number of essential minerals (n), making this matrix square. Matrix C ($n \times n$) can then be inverted (Equation E7; Strang, 1993); during inversion, the row and column labels of matrices C and C^{-1} swap sides.

$$C = \underset{\text{Minerals}}{} \begin{pmatrix} \overset{\text{Elements}}{c_{11}} & \cdots & c_{1n} \\ \vdots & \ddots & \vdots \\ c_{n1} & \cdots & c_{nn} \end{pmatrix} \rightarrow C^{-1} = \underset{\text{Elements}}{} \begin{pmatrix} \overset{\text{Minerals}}{c_{11}^{-1}} & \cdots & c_{1n}^{-1} \\ \vdots & \ddots & \vdots \\ c_{n1}^{-1} & \cdots & c_{nn}^{-1} \end{pmatrix} \qquad \text{(E7)}$$

The second step in this procedure involves conversion of the mass-based element concentrations (those in matrix C), already in matrix form with samples (p) along the side and element concentrations (n) along the top, into unstandardized molar element numbers via column division by the corresponding molecular weights, producing matrix E (also $p \times n$; Equation E8).

$$\underset{\text{Samples}}{} \begin{pmatrix} \overset{\text{Elements}}{e_{11}} & \cdots & e_{1n} \\ \vdots & \ddots & \vdots \\ e_{p1} & \cdots & e_{pn} \end{pmatrix} \times \underset{\text{Elements}}{} \begin{pmatrix} \overset{\text{Minerals}}{c_{11}^{-1}} & \cdots & c_{1n}^{-1} \\ \vdots & \ddots & \vdots \\ c_{n1}^{-1} & \cdots & c_{nn}^{-1} \end{pmatrix} = \underset{\text{Samples}}{} \begin{pmatrix} \overset{\text{Minerals}}{m_{11}} & \cdots & m_{1n} \\ \vdots & \ddots & \vdots \\ m_{p1} & \cdots & m_{pn} \end{pmatrix} \qquad \text{(E8)}$$

Then, matrix multiplication is used to 'change the basis' of how the rock compositions are described, from elements to minerals. This is undertaken by multiplying matrix E by the inverse of matrix C to produce a matrix M containing unstandardized molar mineral numbers ($E \times C^{-1} = M$; Equation E8). Note that in this matrix equation, the 'inner' dimensions of matrices E and C^{-1} must correspond [$(p \times n) \bullet (n \times n) = (p \times n)$]. Also, not coincidentally, the 'inner' units of the E and C^{-1} matrices correspond [(*samples* × *elements*) $\bullet$ (*elements* × *minerals*) = (*samples* × *minerals*)].

The resulting unstandardized molar mineral numbers can then be converted into unstandardized volume mineral numbers or into unstandardized mass mineral numbers, interchangeably, using the densities, molecular weights, and molar volumes (equal to mineral density/molecular weight) of the essential minerals, as illustrated in Figure 7. Finally, these unstandardized numbers can be standardized by summing the numbers for each sample and dividing these numbers by the sum to 'close' the data (ensuring that these modal mineral concentrations, in whatever

form, sum to unity):

$$\frac{x_1}{\sum_{i=1}^{n} x_i}, \frac{x_2}{\sum_{i=1}^{n} x_i}, \frac{x_3}{\sum_{i=1}^{n} x_i}, \cdots, \frac{x_n}{\sum_{i=1}^{n} x_i}. \qquad (E9)$$

All of the above calculations can easily be implemented in Excel®.

EXAMPLES

The following five case histories illustrate how the four MER lithogeochemical data analysis tools can be used in a variety of mineral industry applications. In all cases, data quality assessment samples (blanks, reference materials, and duplicates) were used to ensure that the data are accurate, precise, and, in cases where multiple datasets were examined together, leveled. Results of these evaluations demonstrate that datasets used in the following case histories are 'fit for purpose' (Bettaney and Stanley, 2001).

Hanson Lake Assemblage, Saskatchewan

Mining companies have actively explored for volcanic hosted massive sulphide (VHMS) deposits in the Flin Flon greenstone belt (FFGB) of Manitoba and Saskatchewan for many years (Wright and Stockwell, 1934; Byers, 1957; Gaskarth, 1967; Coleman et al., 1970; Parslow and Gaskarth, 1986; Sibbald, 1989; Kozial and Ostapovitich, 1993; Stern et al., 1995; Syme et al., 1998). In Saskatchewan, important discoveries were made in both the Hanson Lake and Northern Lights Assemblages of the FFGB, and include the Western Nuclear Pb-Zn VHMS deposit, discovered by the Parrex Bay Mining Syndicate in 1957 and mined in the 1960s, and McIlvenna Bay and Bigstone Cu-Zn VHMS deposits, discovered in 1988 and 1983 by the Saskatchewan Mining Development Agency (SMDC) and a Granges/SMDC joint venture, respectively, both of which remain un-mined to date.

Unfortunately, Paleozoic sedimentary rocks lap onto the greenstone belt to the south, obscuring the prospective Paleoproterozoic rocks, and imposing major challenges to mineral exploration. Diamond drilling of geophysical targets south of the unconformity has proven to be at least partially effective, as several deposits have been discovered by these means. Nevertheless, many exploration programs have been unsuccessful, in part because a detailed understanding of the volcano-sedimentary stratigraphy has not been available to help guide exploration.

In the exposed portion of the FFGB on the shores of Hanson Lake, Saskatchewan, rocks strike north-south, face east, and extend under the Paleozoic unconformity. Regional mapping by Maxeiner et al., (1993, 1995, 1999) provides a good understanding of the lithostratigraphy for that portion of the greenstone belt. The sequence consists mostly of mafic volcanic rocks to the west, overlain by a thick package of dacite, then rhyolite, and finally turbiditic metasedimentary rocks that have been intruded by synvolcanic quartz-feldspar porphyry intrusives, synsedimentary diorite sills, and later gabbro and granite. Unfortunately, the large-scale resolution of this mapping is generally unable to assist diamond drill-core interpretation and prospect targeting under cover to the south, a feature that is further undermined by the greenschist-to-amphibolite grade metamorphism that occurs in the area.

As a result, Foran Mining Corporation funded a major oxide lithogeochemical mapping research project in the Hanson Lake area (Kramar, 2017) to provide additional chemostratigraphic information. When combined with data from Maxeiner's lithostratigraphic mapping, this provided Foran with an improved, fine-scale understanding of the stratigraphy, thereby enhancing their ability to properly interpret diamond drill-core information in areas lacking outcrop.

Kramar (2017) collected 378 samples from outcrops in the Hanson Lake study area, and combined these with historical lithogeochemical data (n = 980) from Maxeiner et al., (1995, 1999), other mappers/researchers (Parslow and Gaskarth, 1986; Morelli, 2012; Morelli and Maxeiner, 2014), and mineral exploration companies active in the area over the past 30 years (Kreczmer and Koch, 1983; Koziol and Stoeterau, 1984; Koziol, 1985; Sopuck and Duncan, 1990). Kramar identified and correlated a number of new units within the stratigraphy not previously recognized using the conserved element analysis procedures identified above.
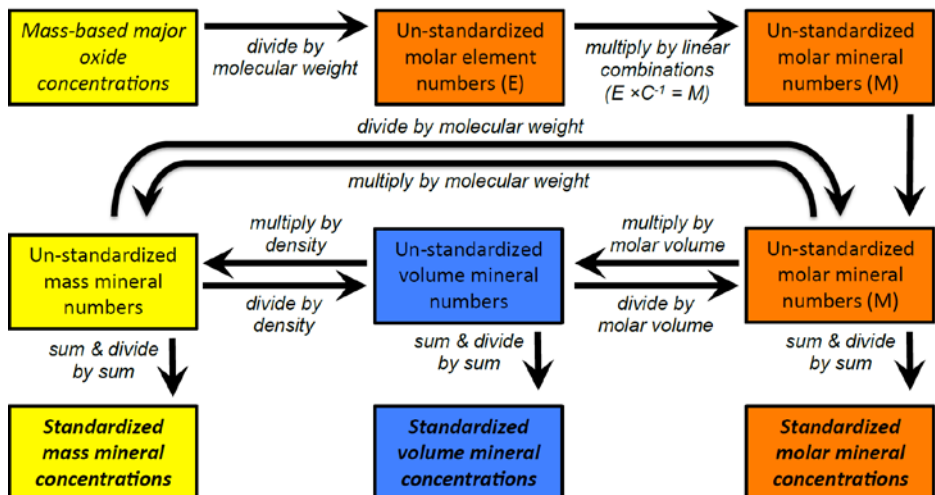

Figure 7: Graphical illustration of the calculation scheme to undertake the change of basis rock classification procedure (Stanley, 2017) that converts element concentrations into mineral concentrations. Densities, molecular weights and molar volumes are used to convert between mass, mole and volume concentration units. Element concentrations can only be described in mass (yellow) and mole (orange) terms, whereas mineral concentrations can be described in mass (orange), mole (yellow), and volume (blue) terms.

Results provide an enhanced understanding of the stratigraphy, and substantially improve its resolution to facilitate drill-core interpretation and targeting. Specifically, the original 'dacite' unit in the study area could be sub-divided into interbedded rhyolite and rhyodacite units with interbedded banded Fe formation. Furthermore, the original 'rhyolite' unit above this 'dacite' could be subdivided into two different and distinct rhyolite units (Figures 8 and 9). All of these felsic lithologies contain variable proportions of quartz and feldspar in a range of sizes, but do not exhibit petrographic differences significant enough to confidently be used to discriminate between these units. Consequently, it appears that lithogeochemistry is the only means to map these otherwise cryptic lithologies.
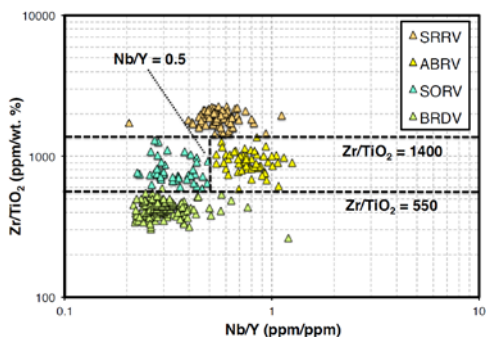
Figure 8: Conserved element log-ratio diagram of felsic rocks from the Hanson Lake Assemblage (data from Kramar, 2017). Two Zr/TiO_2 thresholds and one Nb/Y threshold distinguish four different felsic volcanic rock compositions within the Hanson Lake Assemblage stratigraphy. BRDV - Bertram Bay Rhyodacite volcanic (n = 265), SORV - South Bay Rhyolite volcanic (n = 98), ABRV - Agnew Bay Rhyolite volcanic (n = 79), and SRRV - Sareco Bay Rhyolite volcanic (n = 127).
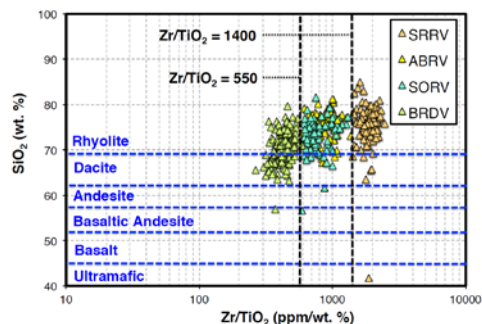

Figure 9: Diagram of Zr/TiO_2 (log scale) plotted against SiO_2 (data from Kramar, 2017). Because of the overall low level of hydrothermal alteration, SiO_2 concentrations in these rocks are largely un-modified, and can be used to provide names for these volcanic rocks (per abbreviations in Figure 8).

Two different basalt compositions were also identified, one occurring as a series of flows at the base of the sequence, and the second as another set of flows above the original 'rhyolite' (Figure 10). Finally, a large, sub-volcanic dacite intrusive could be correlated with previously unrecognized eruptive dacite volcanic and epiclastic rocks (Figure 11) that occur within the

penultimate clastic sedimentary unit at the top of the stratigraphy, establishing an important age constraint.

These stratigraphic refinements have led to the recognition of new exploration targets located at several specific stratigraphic levels that could explain the anomalies identified by historic geophysical surveys. Consequently, conserved element analysis has allowed Foran to better interpret rocks and rock sequences within Paleoproterozoic stratigraphy encountered in drill-core south of Hanson Lake, improving their ability to explore beneath the Paleozoic unconformity along strike from, as well as in the footwall and hanging wall of, the McIlvenna Bay VHMS deposit.
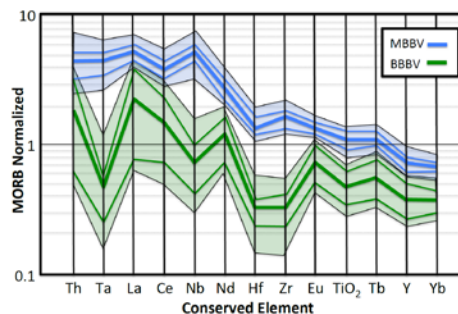

Figure 10: Extended REE spidergram of Bevins et al. (1984) illustrating MORB-standardized conserved element patterns of two basalt units in the Hanson Lake Assemblage (data from Kramar, 2017). BBBV - Bertram Bay Basalt volcanic (n = 17), and MBBV - Mine Bay Basalt volcanic (n = 83). For each unit, thick line, thin lines, and the shaded zone define the average, 25th and 75th percentile, and 5th and 95th percentile standardized concentrations.
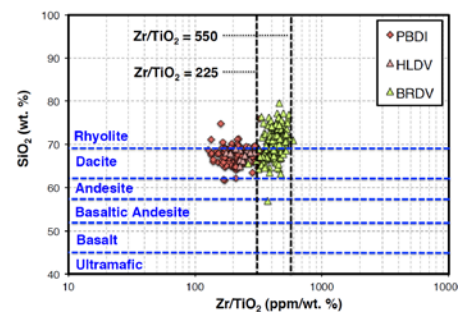

Figure 11: Diagram of Zr/TiO_2 (log scale) plotted against SiO_2 (data from Kramar, 2017). As in Figure 9, SiO_2 concentrations in these rocks are largely un-modified, and can be used to provide names to these volcanic and hypabyssal rocks. Abbreviations: HLDV - Hanson Lake Dacite volcanic (n = 16); PBDI – Parrex Bay Diorite intrusive (n = 234); BRDV – Bertram Bay Rhyodacite volcanic (n = 265).

United Verde VHMS Deposit, Arizona

The United Verde VHMS deposit is hosted by Proterozoic felsic volcanic rocks of the Ash Creek Block, Yavapai Series exposed on the margin of the Colorado Plateau outside of Jerome, Arizona. These rocks consist of flows, tuffs, breccias,

volcaniclastic rocks, bedded cherts and exhalative ironstones cut by hypabyssal porphyries, collectively exhibiting a full range of volcanic rock compositions. The stratigraphy includes the basal Gaddes Basalt, Buzzard Rhyolite, Burnt Canyon Dacite, Deception Rhyolite and the overlying Grapevine Gulch Formation (Vance and Condie, 1987; Vance, 1989; Gustin, 1988, 1990).

Mining of the polymetallic United Verde ore body took place between 1883 and 1957, and an early understanding of the deposit was provided by Anderson and Creasey (1958) and Alenius (1968). However, little was known about the nature of hydrothermal alteration and its zoning, nor the environment of deposition of this mineralization. As a result, two Ph.D. thesis projects were undertaken in the United Verde area to gain a modern understanding of its hydrothermal alteration and geological setting (Vance and Condie, 1987; Vance, 1989; Gustin, 1988, 1990).

Both thesis studies involved the collection of samples from surface and drill-core. Lithogeochemical analyses from these theses have been compiled into a dataset of 85 felsic volcanic rock samples. Lithologies represented by these samples include: (i) the Buzzard Rhyolite (n = 11), a 1000 m thick package of fresh flows and volcaniclastic rocks, (ii) the Burnt Canyon Dacite (n = 11), a 600 m thick package of fresh flows, and (iii) the host Deception Rhyolite (n = 63), a 1200 m thick package of variably hydrothermally altered flows, tuffs, breccias and self-intruding quartz-feldspar porphyry. At United Verde, the Deception Rhyolite is divided into Lower, Cleopatra, and Upper Members, and mineralization occurs at the top of the Cleopatra Member (Anderson and Creasey, 1958).

Figure 12 investigates the conserved element behavior of these felsic rocks. On this diagram, both TiO_2 and Zr exhibit constant and distinguishing ratios in the three lithological units. Additionally, all samples have SiO_2 concentrations consistent with their unit names, except for some samples of Deception Rhyolite (in green) that have extremely low SiO_2 concentrations. These samples exhibit intense chlorite alteration and occur in the immediate footwall to mineralization. Because these rocks are composed only of chlorite, they should probably be referred to as 'chloritite', but have been historically referred to as 'black schist' by miners (Anderson and Creasey, 1958).

Figure 13 presents a PER diagram used to investigate hydrothermal alteration in alkali feldspar-bearing rocks. Burnt Canyon Dacite, Buzzard Rhyolite and some Deception Rhyolite rocks plot along the alkali feldspar control line, indicating that they are relatively unaltered, and that their feldspar does not contain a significant anorthite component. However, some Deception Rhyolite samples plot below the alkali feldspar control line, and thus appear to be hydrothermally altered. These samples define two trends on Figure 13.

The first trend extends from the alkali feldspar control line downward across the muscovite control line to the chlorite control line, and so tracks the effects of the feldspar-to-muscovite (blue arrow) and muscovite-to-chlorite (brown arrow) alteration reactions. The second trend is horizontal, defined by samples that plot along the horizontal axis (red arrow). This data

trend is defined by the chloritite samples with low SiO_2 concentrations from the Deception Rhyolite (Figure 12). Consequently, this trend likely tracks a second chlorite-forming reaction.
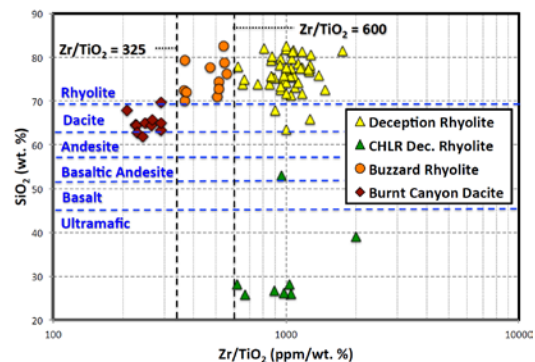

Figure 12: Conserved element diagram of Zr/TiO_2 (log scale) plotted against SiO_2 for lithogeochemical samples from the United Verde VHMS camp. Vertical lines separate lithologies defined by natural thresholds in Zr/TiO_2 ratios.
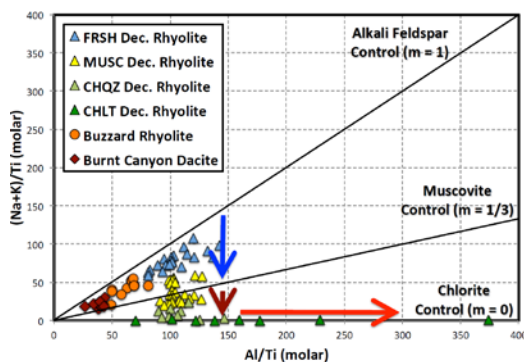

Figure 13: PER diagram of Al/Ti plotted against (Na+K)/Ti for lithogeochemical samples from the United Verde VHMS camp. Some samples from the Deception Rhyolite are likely muscovite and chlorite altered, because they plot below the alkali feldspar control line.

Figure 14 presents a GER diagram plotting (Na+K)/Al versus Na/Al that further investigates the muscovite- and chlorite-forming reactions in these rocks. On this diagram, Deception Rhyolite samples plot along two trends, one between the albite and muscovite nodes (blue arrow), and the second between the muscovite and chlorite nodes (brown arrow). These illustrate that the muscovite alteration affected these rocks first, followed by chlorite alteration, and that the predominant feldspar in fresh Deception Rhyolite, Buzzard Rhyolite and Burnt Canyon Dacite samples is albite.
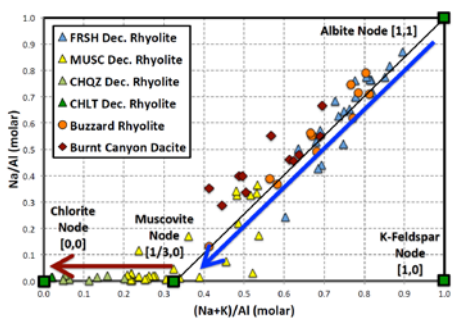
Figure 14: GER diagram plotting (Na+K)/Al versus Na/Al for lithogeochemical samples from the United Verde VHMS camp. The data form trends illustrating that muscovite alteration of albite preceded chlorite alteration of muscovite.

Figures 15, 16 and 17 present complementary GER diagrams plotting (Na+K)/Al versus K/Al, (Fe+Mg)/Al and Si/Al, respectively. Figure 15 exhibits two data trends demonstrating that Deception Rhyolite samples underwent K addition (blue arrow) during muscovite alteration, but then K loss (brown arrow) during chlorite alteration.
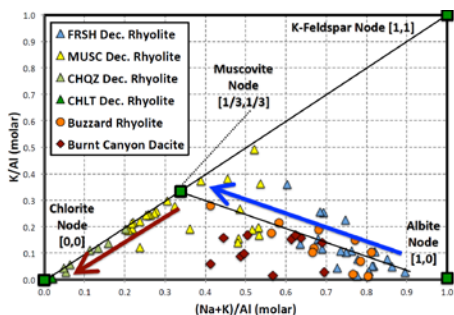
Figure 15: GER diagram of (Na+K)/Al plotted against K/Al for lithogeochemical samples from the United Verde VHMS camp. The data form two trends that indicate K was first added and then removed from Deception Rhyolite samples during hydrothermal alteration.
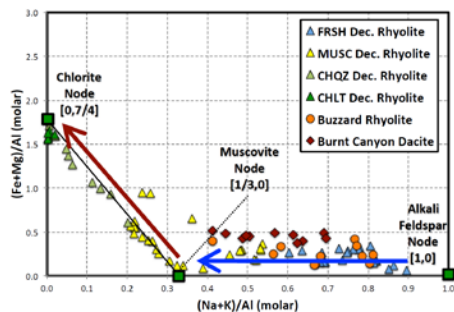

Figure 16: GER diagram of (Na+K)/Al plotted against (Fe+Mg)/Al for lithogeochemical samples from the United Verde VHMS camp. This diagram constrains chlorite to have a composition with a (Fe+Mg)/Al ratio of 7/4.
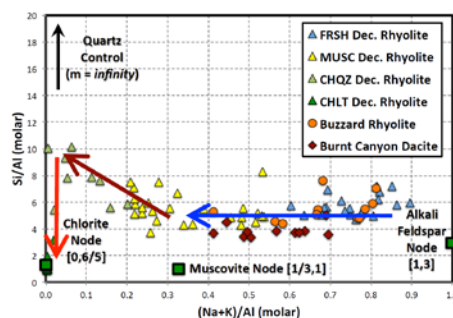

Figure 17: GER diagram of (Na+K)/Al plotted against Si/Al for lithogeochemical samples from the United Verde VHMS camp. The data form three trends indicative of three styles of hydrothermal alteration at United Verde.

Similarly, Figure 16 exhibits analogous trends corresponding to muscovite (blue arrow) and chlorite (brown arrow), and indicates that the chlorite in Deception Rhyolite samples has an (Fe+Mg)/Al ratio of 7/4. The formula for this intermediate chlorite composition can be derived by adding sufficient tschermak exchange component $[Al_2(Fe,Mg)_{-1}Si_{-1}]$ (2/3 moles) to an additive component of ideal clinochlore/chamosite $[(Fe,Mg)_{10}Al_4Si_6O_{20}(OH)_{16}]$ to produce a (Fe+Mg)/Al ratio of 7/4 (Thompson, 1982; Burt, 1988, 1994). The resulting chlorite composition $[(Fe,Mg)_{28/3}Al_{16/3}Si_{16/3}O_{20}(OH)_{16}]$ has a Si/Al ratio of unity, exactly equal to that of muscovite, suggesting that muscovite may exert a control on the composition of chlorite that formed from it.

Finally, Figure 17 exhibits three distinct trends representing the three different styles of hydrothermal alteration that have affected these rocks. It illustrates that no significant Si metasomatism took place during the muscovite alteration of albite (blue arrow), but Si was apparently added during chlorite alteration of muscovite (brown arrow), probably via quartz precipitation. Interestingly, despite a trend suggesting that Si was lost during alteration to chloritite (red arrow), it is possible that Al addition, as observed in chloritite samples in Figure 13, is responsible for the lower Si/Al ratios exhibited by Deception Rhyolite chloritite samples in Figure 17.

To confirm whether this is true, a PER diagram plotting Al/Ti versus Si/Ti was constructed (Figure 18). On this diagram, all Burnt Canyon Dacite, Buzzard Rhyolite and most Deception Rhyolite samples plot well above the Deception Rhyolite 'chloritite' samples, suggesting that these chloritite samples lost Si during this third hydrothermal alteration reaction (red arrow). As a result, Si loss and Al addition must jointly be responsible for the decreasing Si/Al ratios in the chloritite-altered samples on Figure 17.
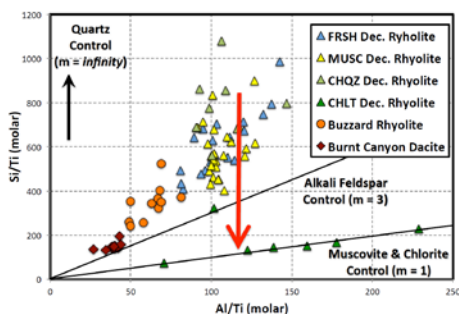
Figure 18: GER diagram plotting (Na+K)/Al versus Si/Al for lithogeochemical samples from the United Verde VHMS camp. Chloritite samples (green) have lost Si during the formation of chlorite, and exhibit a Si/Al ratio exactly equal to muscovite from which they form.
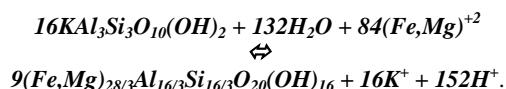
Interestingly, on Figure 18, Deception Rhyolite samples plot precisely on the muscovite/chlorite control line, exhibiting Si/Al ratios of unity. Because these chloritite samples contain only chlorite, their bulk Si/Al ratio must equal the Si/Al ratio of the chlorite in these samples. This confirms that the chlorite composition in chloritite is exactly equal to that derived using the clinochlore/chamosite additive component and tschermak exchange component, above $[(Fe,Mg)_{28/3}Al_{16/3}Si_{16/3}O_{20}(OH)_{16}]$ (Thompson, 1982; Burt, 1988, 1994).

With the above constraints provided by Figures 13-18, the actual geochemical reactions responsible for hydrothermal alteration in the Deception Rhyolite can be determined. The first reaction is balanced on Al, because the vertical trend on Figure 13 indicates that Al was neither added nor removed during this alteration. As a result, the alteration reaction describing how albite altered to muscovite plus quartz (blue arrows in Figures 13-17) is:

$$3NaAlSi_3O_8 + K^+ + 2H^+ \Leftrightarrow KAl_3Si_3O_{10}(OH)_2 + 6SiO_2 + 3Na^+.$$

During this albite-to-muscovite alteration, Na was lost (Figure 14), K (Figure 15) and H were added, and quartz precipitated, despite the fact that Si was not added (note that this is likely because, where this alteration took place, the hydrothermal fluid was already silica saturated).
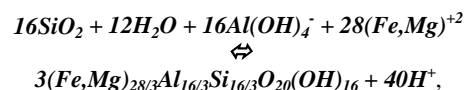
The second reaction, also balanced on Al, involves the alteration of muscovite to chlorite (brown arrows in Figures 13-17):

$$16KAl_3Si_3O_{10}(OH)_2 + 132H_2O + 84(Fe,Mg)^{+2}$$
$$\Leftrightarrow$$
$$9(Fe,Mg)_{28/3}Al_{16/3}Si_{16/3}O_{20}(OH)_{16} + 16K^+ + 152H^+.$$

During this muscovite-to-chlorite alteration, K was lost (Figure 15), and Fe+Mg (Figure 16) and H were added. Furthermore, in contrast to the albite-to-muscovite reaction above, this reaction does not involve silica. Nevertheless, Si was added (likely as the direct precipitation of quartz open spaces; per Figure 17).

The third reaction can also be balanced, but in this case, not because Al is conserved. Instead, a different constraint, the final chlorite composition was used. This chlorite has an (Fe+Mg)/Al ratio of 7/4, so the amount of Fe+Mg addition that occurred during this reaction must be 7/4 times the amount of Al addition

to ensure that the (Fe+Mg)/Al ratios of the chloritite samples remain equal to 7/4. Consequently, this chloritite-forming reaction is:

$$16SiO_2 + 12H_2O + 16Al(OH)_4^- + 28(Fe,Mg)^{+2}$$
$$\Leftrightarrow$$
$$3(Fe,Mg)_{28/3}Al_{16/3}Si_{16/3}O_{20}(OH)_{16} + 40H^+,$$

and can be thought of as a quartz-to-chlorite reaction (red arrows in Figures 13, 17, 18).

Using the above balanced reactions, one can calculate the volume changes that occurred during hydrothermal alteration using the molar volumes (equal to mineral densities/molecular weights) of the solid phases on each side of each reaction. As albite altered to muscovite, volume decreased by 8% (blue arrows in Figures 13–17). This volume loss caused open space to be produced, allowing the influx of more hydrothermal fluid, that then caused more alteration, and thus more open space, *et cetera*, in a self-perpetuating cycle. This explains why muscovite alteration in many VHMS systems is typically so widespread.

In contrast, the muscovite-to-chlorite alteration reaction (brown arrows in Figures 13-17) involves a substantial volume gain of 39% to 76%, depending on the Mg # of the chlorite. As a result, any open space that was initially available was quickly filled, reducing the porosity and self-limiting the reaction. This explains why chlorite alteration in most VHMS systems is typically very local, limited to places where significant open space exists, such as at or near the sea floor, or within sub-vertical fractures that serve as conduits for the hydrothermal fluids. At United Verde, the addition of Si, likely via the precipitation of quartz during this reaction (brown arrow, Figure 17), further added to this volume gain, and thus further limited the spatial extent of this chlorite alteration.

Lastly, the chloritite-producing quartz-to-chlorite alteration reaction exhibits a substantial volume increase of between 186% and 264%, depending on the Mg # of the chlorite. The very substantial volume gain associated with this reaction likely explains why it is restricted to the seafloor, immediately beneath the United Verde mineralization, where substantial open space was available. Additional open space to allow this reaction to reach completion (*i.e.* pure chlorite) was likely created by the loss of Si that co-occurred during this reaction (Figure 17), as quartz dissolution. Consequently, conditions where this alteration took place differed from those of the first two reactions, as here quartz was under-saturated and Al was soluble in the hydrothermal fluid, whereas conditions where the first two reactions occurred were quartz-saturated and Al was relatively insoluble.

The above analysis of hydrothermal alteration at the United Verde VHMS deposit not only provides important details about how the hydrothermal alteration system evolved, but provides important information about a new hydrothermal alteration zone in VHMS deposits, explains controls on the spatial distribution of different hydrothermal alteration zones and provides constraints regarding the conditions under which these hydrothermal alteration reactions took place. All of these features provide important new information that refines our

understanding of a genetic model for VHMS mineralization, and so provides several advantages to mineral exploration for such deposits.

Duluth Igneous Complex Cu-Ni Deposit, Minnesota

The Mesoproterozoic (Keweenawan) Duluth Igneous Complex in northeastern Minnesota is host to as many as ten Ni-Cu sulphide deposits located at the base of the Partridge River and South Kawishiwi intrusions on the western edge of the complex. The associated magmas intruded beneath earlier anorthosite and are host to disseminated, Cu-Ni-rich mineralization. The magmas are layered and comprised of gabbros, troctolites, mela-troctolites and anorthosites. Norites occur where the magmas have digested iron formation wall rock xenoliths (Miller, 2011).

Exploration in this area over the past 70 years by more than 25 companies has produced more than 1000 drill-cores, a major proportion of which are held in archive in the Minnesota Department of Natural Resources drill-core library in Hibbing, Minnesota (Severson and Hauck, 2008). Since 1998, these have been re-logged by geologists from the Natural Resources Research Institute, University of Minnesota, Duluth to improve understanding of the controls on mineralization and the distribution of PGE-bearing minerals.

Subtle molar mineral differences distinguish the lithologies in these olivine tholeiite intrusions. Unfortunately, given a project of this size, inherent inaccuracies can be expected in the drill-core logs because of inconsistencies between the many drill-core loggers, and daily variations in modal estimates of minerals (olivine, plagioclase, clinopyroxene, orthopyroxene, sulphide minerals, oxide minerals) can occur. These errors can substantially distort conclusions about the character and genesis of the deposits (Severson and Hauck, 2008). Consequently, to confirm drill-core logging accuracy, 99 samples from 14 cores drilled in 2013 were collected and analyzed by Twin Metals Minnesota LLC from the South Kawishiwi Intrusion, and subjected to a MER analysis, including classification using the change of basis procedure (Stanley, 2017).

The first step in this analysis was the identification of conserved elements. Figure 19 presents a scatterplot of Zr plotted against Nb. Samples plot crudely along a line that passes through the origin, confirming that these elements are conserved, and that these rocks are cogenetic (derived from parent rocks of common composition).
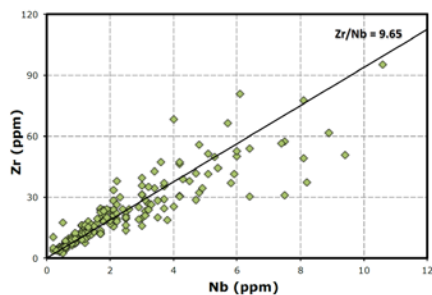

Figure 19: Conserved element scatterplot of Nb versus Zr for 99 South Kawishiwi Intrusion drill-core samples.

Figures 20, 21, and 22 are PER diagrams investigating the nature of compositional variations in these rocks. Figure 20 plots Si/Zr versus (Fe/2+Mg/2)/Zr and thus tests the hypothesis of olivine sorting. Because samples plot close to the horizontal axis, and do not plot along the olivine control line, this hypothesis is rejected. Figure 21 plots Si/Zr versus (2Ca+3Na)/Zr and thus tests the hypothesis of plagioclase and clinopyroxene sorting. Because most samples plot just below the plagioclase control line, this hypothesis is also rejected. Figure 22 plots Si/Zr versus (Fe/2+Mg/2+2Ca+3Na)/Zr and thus tests the hypothesis of olivine **and** plagioclase sorting. On this diagram, samples plot along the olivine and plagioclase control line, indicating that sorting of these minerals can explain the compositional variability in these samples.

South Kawishiwi Intrusion samples were also investigated using GER diagrams. Figure 23 presents a GER diagram with axes of Mg/Si plotted against Ca/Si. On this diagram, olivine compositions plot on the horizontal axis, whereas plagioclase compositions plot along the vertical axis. Samples plot between the median olivine and plagioclase compositions in these rocks, as determined by 1646 and 2278 electron microprobe analyses of these minerals, respectively (assembled from a variety of published and unpublished sources by Twin Metals Minnesota LLC), indicating that these rocks are mostly mixtures of olivine and plagioclase (*i.e.*, troctolites).
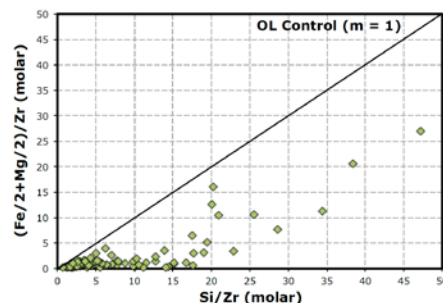

Figure 20: PER diagram of Si/Zr plotted against (Fe/2+Mg/2)/Zr for 99 lithogeochemical samples from South Kawishiwi Intrusion drill-core. Olivine sorting alone cannot explain the compositional variations in these rocks.
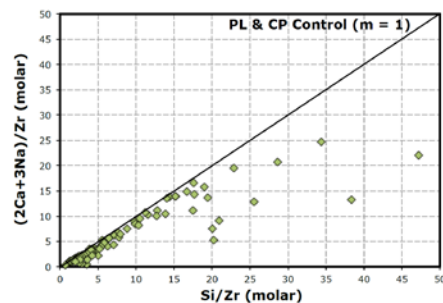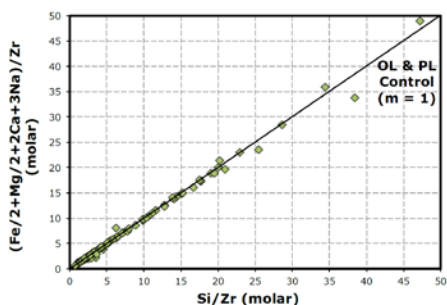

Figure 21: PER diagram of Si/Zr plotted against (2Ca+3Na)/Zr for 99 lithogeochemical samples from South Kawishiwi Intrusion drill-core. Plagioclase sorting alone cannot explain the compositional variations in these rocks.

Figure 22: PER diagram of Si/Zr plotted against (Fe/2+Mg/2+2Ca+3Na)/Zr for 99 lithogeochemical samples from South Kawishiwi Intrusion drill-core. Olivine and plagioclase sorting explain the compositional variations in these rocks.
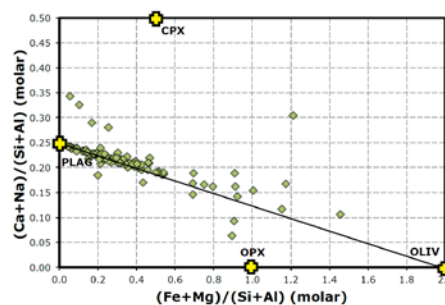
Figure 24 plots a second GER diagram with axes of (Fe+Mg)/(Si+Al) plotted against (Ca+Na)/(Si+Al). On this diagram, all possible olivine compositions plot at [2,0], whereas all possible plagioclase compositions plot at [0,1/4]. Samples plot on the join between these two nodes, and those plotting closer to the plagioclase node are anorthosites and leuco-troctolites, whereas those plotting closer to the olivine node are mela-troctolites and dunites. Outlying samples likely contain olivine and plagioclase, plus other minerals such as orthopyroxene, clinopyroxene and magnetite. Although classification of these rocks could be undertaken using this diagram, the modal proportions derived from it would be in molar terms, and thus would be unsuitable for classification unless converted into volume proportions.

Lastly, Figure 25 presents a GER diagram with axes of (Si-Al/2-3Na/2)/(Si-2Al+3Ca) plotted against (Si/4+Al/4+3Fe/8+3Mg/8)/(Si-2Al+3Ca). On this diagram, all compositions of both plagioclase and olivine plot at [1,1]. Consequently, most samples plot at or close to this node, but some are displaced toward the clinopyroxene node, indicating that they likely contain small amounts of clinopyroxene, and have gabbroic affinity.
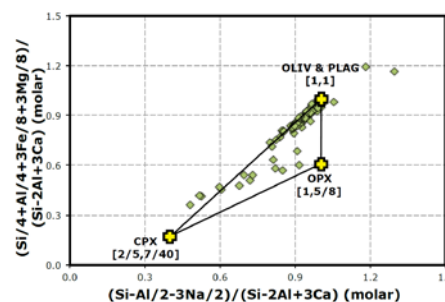

Figure 23: GER diagram of Mg/Si plotted against Ca/Si for 99 drill-core samples from the South Kawishiwi Intrusion. Most samples plot on a mixing line between FO61 and AN58.

Figure 24: GER diagram of (Fe+Mg)/(Si+Al) plotted against (Ca+Na)/(Si+Al) for drill-core samples from the South Kawishiwi Intrusion. Most samples have compositions of anorthosite or leuco-troctolite.

Figure 25: GER diagram of (Si-Al/2-3Na/2)/(Si-2Al+3Ca) plotted against (Si/4+Al/4+3Fe/8+3Mg/8)/(Si-2Al+3Ca) for drill-core samples from the South Kawishiwi Intrusion. Some samples plot between the clinopyroxene and olivine/plagioclase nodes, indicating that they have gabbroic affinities.

As a final step in the analysis of South Kawishiwi Intrusion drill-core samples, a change of basis classification (Stanley, 2017) was undertaken using the essential mineralogy of the rocks. Because these rocks are olivine tholeiites, this essential mineral assemblage includes olivine (OLIV), plagioclase (PLAG), clinopyroxene (CLPX) and orthopyroxene (ORPX), but some rocks have essential chromite (CHRM), apatite (APAT), and titanomagnetite and sulphide minerals. As a result, magnetite (MAGT) and ulvospinel (ULVO) were used to describe titanomagnetite, and troilite (PYRH), chalcopyrite (CHPY) and millerite (MILL) were used to describe the sulphide minerals; K-feldspar was included as a component in plagioclase. The compositions of these essential minerals were placed in a matrix (C; Equation E10). This was inverted to produce the linear combinations necessary to convert the unstandardized molar element numbers into unstandardized molar mineral numbers, as part of the change of basis classification procedure (Stanley, 2017).
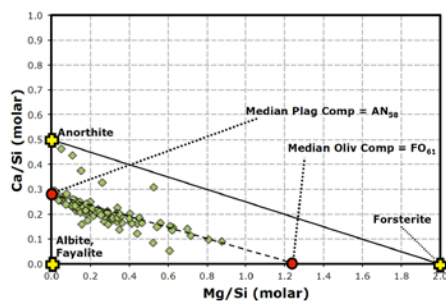
$$
\begin{array}{r}
\quad\quad\quad\quad Si\ Al\ FM\ Ca\ Na\ K\ Cr\ Fe^{+3}\ P\ Ti\ S\ Cu\ Ni \\
\begin{array}{r}
OLIV \\ ORPX \\ CLPX \\ ANOR \\ ALBT \\ KSPR \\ C = \quad CHRM \\ MAGT \\ ULVO \\ APAT \\ PYRH \\ CHPY \\ MILL
\end{array}
\left[
\begin{array}{ccccccccccccc}
1 & 0 & 2 & 0 & 0 & 0 & 0 & 0 & 0 & 0 & 0 & 0 & 0 \\
2 & 0 & 2 & 0 & 0 & 0 & 0 & 0 & 0 & 0 & 0 & 0 & 0 \\
2 & 0 & 1 & 1 & 0 & 0 & 0 & 0 & 0 & 0 & 0 & 0 & 0 \\
2 & 2 & 0 & 1 & 0 & 0 & 0 & 0 & 0 & 0 & 0 & 0 & 0 \\
3 & 1 & 0 & 0 & 1 & 0 & 0 & 0 & 0 & 0 & 0 & 0 & 0 \\
3 & 1 & 0 & 0 & 0 & 1 & 0 & 0 & 0 & 0 & 0 & 0 & 0 \\
0 & 0 & 1 & 0 & 0 & 0 & 2 & 0 & 0 & 0 & 0 & 0 & 0 \\
0 & 0 & 1 & 0 & 0 & 0 & 0 & 2 & 0 & 0 & 0 & 0 & 0 \\
0 & 0 & 2 & 0 & 0 & 0 & 0 & 0 & 0 & 1 & 0 & 0 & 0 \\
0 & 0 & 0 & 5 & 0 & 0 & 0 & 0 & 3 & 0 & 0 & 0 & 0 \\
0 & 0 & 1 & 0 & 0 & 0 & 0 & 0 & 0 & 0 & 1 & 0 & 0 \\
0 & 0 & 1 & 0 & 0 & 0 & 0 & 0 & 0 & 0 & 2 & 1 & 0 \\
0 & 0 & 0 & 0 & 0 & 0 & 0 & 0 & 0 & 0 & 1 & 0 & 1
\end{array}
\right]
\end{array}
\quad\text{(E10)}
$$

Results are plotted on an olivine-pyroxene-plagioclase volume classification diagram (Streckeisen et al., 2002; Figure 26). These are consistent with Figures 23 and 24, as most samples classify as anorthosites or leuco-troctolites. However, because some samples classify as gabbros or norites, samples have also been plotted on a clinopyroxene-orthopyroxene-plagioclase volume classification diagram (Streckeisen et al., 2002; Figure 27).

Samples that plot as 'gabbro/norites' on Figure 27 typically occur at the intrusion boundaries or adjacent to hornfelsed mega-inclusions, suggesting that Si contamination from the host rocks resulted in the crystallization of orthopyroxene instead of olivine. In contrast, the leuco-gabbros are likely fractionation products evolved from anorthosite and leuco-troctolite.

Lastly, these quantitative mineral modes have a number of additional applications that can improve understanding of processes that influenced mineral deposit genesis in the Duluth Complex, as well as assisting the exploration efforts made toward new discoveries in the camp. Firstly, these data provide significant aid to mapping and drill-core logging, thereby improving correlation of lithologies on maps and cross-sections.
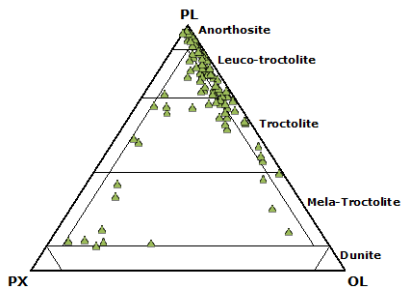

Figure 26: Olivine-pyroxene-plagioclase ternary classification diagram (Streckeisen et al., 2002) for South Kawishiwi Intrusion drill-core samples. Most samples classify as anorthosite and leuco-troctolite.
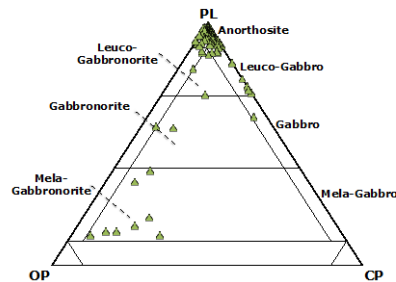

Figure 27: Clinopyroxene-orthopyroxene-plagioclase ternary classification diagram (Streckeisen et al., 2002) for South Kawishiwi Intrusion drill-core samples. The small number of samples that do not classify as anorthosite or leuco-troctolite classify as leuco-, meso-, or mela-gabbronorites, or as leuco-gabbro or gabbro.

Secondly, down-hole modal variations could reveal new geological features, trends and processes not previously recognized. Lastly, frequency distribution analysis of these highly quantitative mineral modes may also identify natural groups of previously unrecognized lithologies and processes.

For example, Figures 28 and 29 present the frequency distributions of two essential silicate minerals found in these rocks. Several natural groupings amongst these samples are identifiable, and could have important genetic implications, thereby improving our understanding of this important mineral deposit type.
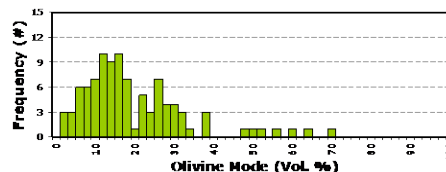

Figure 28: Histograms of calculated olivine mineral modes obtained for 99 South Kawishiwi Intrusion drill-core samples.
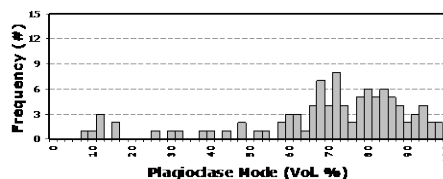

Figure 29: Histograms of calculated plagioclase mineral modes for 99 South Kawishiwi Intrusion drill-core samples.

Phoenix Unconformity U Deposit, Saskatchewan

The Phoenix unconformity uranium deposit is located on the southeast side of the Athabasca Basin, Saskatchewan. Discovered in 2008, it comprises two zones oriented northeast-southwest and is located immediately above the unconformity on the southeast side of a quartzite ridge hanging wall to a sheared graphitic pelite (Roscoe, 2014). The deposit is hosted by the Read Formation, a pink/maroon quartz-rich grit and conglomerate variably interbedded with red siltstone, and

overlain by the Manitou Falls Formation, a maroon to white quartz arenite with interbedded conglomerate in its bottom half, and interbedded siltstone and mudstone and containing mud intraclasts in its upper half (Hiatt and Kyser, 2005).

A total of 253 near-vertical cores have now been drilled into the deposit, and samples for lithogeochemical analysis were collected from 137 of them. These samples are composites of 5 sub-samples collected across 5 m or 10 m intervals (Chen et al., 2015). Digestion was undertaken via a multi-acid (HF/HNO$_3$/HCl) or aqua regia reagent, followed by ICP-ES and ICP-MS analysis. Although 6720 samples were collected, only 4604 were from the Read and Manitou Falls Formations above the unconformity, and these were evaluated using MER analysis (Roscoe, 2014).

Although sedimentary rocks rarely host conserved elements, conserved element analysis of sedimentary rocks has provided new and useful information to explorationists. Figure 30 presents a conserved element scatterplot with TiO$_2$ on the horizontal axis and Zr (ppm) on the vertical axis. Samples do not confirm the presence of conserved elements, but do exhibit a fan-like shape that is commonly observed in clastic sedimentary rocks. As such, samples are bounded by two lines through the origin in a manner that is suggestive of a mixture of two end-member Zr/TiO$_2$ ratios.

In clastic rocks, samples plotting closer to the steeper bounding line (m = 2500; Figure 30) are typically sandstones, probably containing Zr in heavy mineral zircon grains that are concentrated in these coarser facies. In contrast, samples plotting closer to the shallower bounding line (m = 800; Figure 30) are mudstones, probably containing fine-grained leucoxene (a poorly crystalline composite of rutile and Fe-oxy-hydroxide minerals, typically ferrihydrite, goethite, earthy hematite).

The Read and Manitou Falls formations were originally divided into 4 members based on lithofacies characteristics (Ramaekers, 1979, 1980, 1990): (i) basal Member A (the Read Formation) is composed of quartz-rich, polymictic (quartzite, quartzo-feldspathic gneiss, and quartz arenite) conglomerate, with minor sandy mudstone; (ii) Member B is the basal part of the Manitou Falls Formation, consisting of quartz arenite with clast supported conglomerate beds > 2 cm thick; (iii) Member C is the middle part of the Manitou Falls Formation, consisting of quartz arenite with less than 1% mud intraclasts and conglomerate layers < 2 cm thick; and (iv) Member D is the upper part of the Manitou Falls Formation, consisting of well sorted quartz arenite with greater than 1% mud intraclasts. Environmentally, these units were deposited into alluvial fan, proximal and distal braided stream, and estuarine/braid delta environments, from bottom to top (Hiatt and Kyser, 2005).
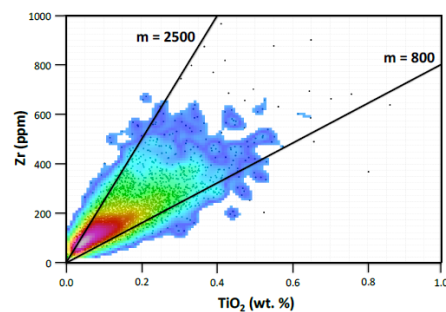

Figure 30: Conserved element scatterplot of TiO$_2$ plotted against Zr for 4604 Read and Manitou Falls Formation samples from above the Phoenix unconformity U deposit, Saskatchewan. Colors correlate with the density of samples in any one part of the graph.

These different members also exhibit different patterns on a TiO$_2$ versus Zr conserved element scatterplot (Figure 31), although the cause(s) for these different patterns remains unknown.
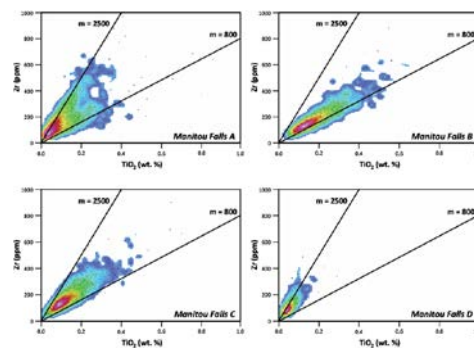

Figure 31: Conserved element scatterplots of TiO$_2$ plotted against Zr for each of the four Read and Manitou Falls Formation lithofacies members for samples from above the Phoenix unconformity U deposit, Saskatchewan. Each member exhibits a different Zr/TiO$_2$ frequency pattern: A – bimodal, B – predominantly low, C – predominantly intermediate, and D – predominantly high.

Without conserved elements, MER analysis of these rocks must be undertaken using GER diagrams. Figures 32 to 35 present several GER diagrams plotting (Na+K)/Al on the horizontal axis against Mg/Al, Fe/Al, Na/Al and K/Al on the vertical axis, respectively. The node locations of common silicate minerals identified in these rocks are also plotted (KAOL = kaolinite; ILLT = illite; FOIT = foititic tourmaline; SUDO = sudoite; Figures 32, 33, 34, 35).
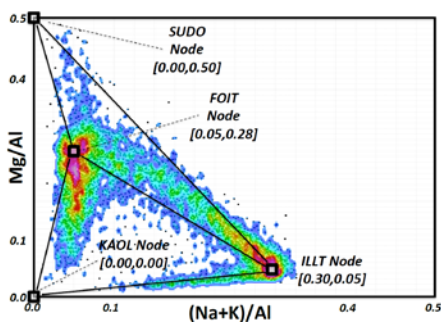
Figure 32: GER diagram plotting (Na+K)/Al against Mg/Al for 4604 Manitou Falls Formation samples from above the Phoenix unconformity U deposit, Saskatchewan.
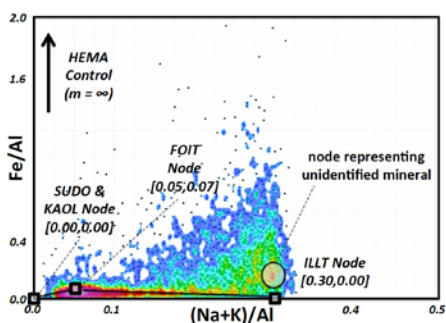

Figure 33: GER diagram plotting (Na+K)/Al against Fe/Al for 4604 Manitou Falls Formation samples from above the Phoenix unconformity U deposit, Saskatchewan.

Two important features are evident on these diagrams. First, there are no rocks with (Na+K)/Al ratios exceeding 1/3. Consequently, there are no rocks containing significant (alkali) feldspar. This feature is uncommon in most clastic sedimentary basins, and could indicate either that an intensely weathered or distal provenance was the source for clastic material in the Athabasca Basin (*cf.* Hiatt and Kyser, 2005), or that diagenesis and hydrothermal alteration served to completely obliterate feldspar from these sedimentary rocks, converting it into clay minerals.

The second feature evident on these figures is that samples exhibit high densities at several points that are close to the nodes of known minerals in these rocks, and the specific locations of these points constrain the actual compositions of these minerals. For example, high sample densities occur at several points with horizontal axis coordinates [(Na+K)/Al, ratios] of 0.30 on Figures 32 to 35, and the mineral responsible for this is likely illite. This horizontal axis coordinate, and the corresponding vertical axis coordinates [the Mg/Al, Fe/Al, Na/Al and K/Al ratios] of 0.04, 0.00, 0.005 and 0.295 specifically define this illite composition. Its formula can be derived by starting with the muscovite additive component $[K_2Al_6Si_6O_{20}(OH)_4]$, and adding to it sufficient amounts of K-edenite exchange component $[K_1Al_1Si_{-1}]$ (1/2 moles), Mg-tschermak exchange component $[Al_2Mg_{-1}Si_{-1}]$ (1/4 moles), and soda-potassic exchange component $[Na_1K_{-1}]$ (1/40 moles) to produce these modal Mg/Al, Fe/Al, Na/Al, and K/Al ratios (Thompson, 1982;

Burt, 1988, 1994). The deduced illite composition $[K_{59/40}Na_{1/40}Mg_{1/4}Al_5Si_{27/4}O_{20}(OH)_4]$ has a Mg-phengite/illite affinity.
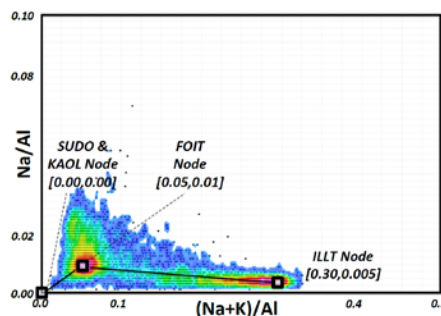

Figure 34: GER diagram plotting (Na+K)/Al against Na/Al for 4604 Manitou Falls Formation samples from above the Phoenix unconformity U deposit, Saskatchewan.
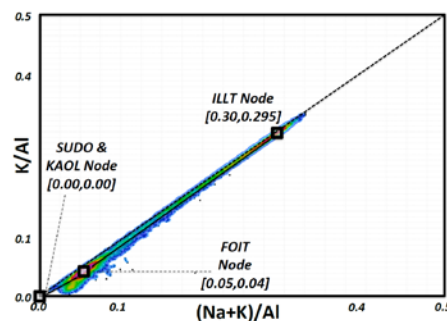

Figure 35: GER diagram plotting (Na+K)/Al against K/Al for 4604 Manitou Falls Formation samples from above the Phoenix unconformity U deposit, Saskatchewan. Colours correlate with the density of samples in any one part of the graph.

Similarly, high sample densities also occur at points with horizontal axis coordinates [(Na+K)/Al ratios] of 0.05. This is likely a tourmaline composition. As above, this horizontal axis coordinate and the corresponding vertical axis coordinates [the Mg/Al, Fe/Al, Na/Al, and K/Al ratios] of 0.28, 0.07, 0.01, and 0.04. These points also specifically define this tourmaline composition. Its formula can be derived by adding to the dravite additive component $[NaMg_3Al_6(BO_3)_3Si_6O_{18}(OH)_4]$ 2/3 moles of foitite exchange component $[Na_{-1}Mg_{-1}Al_1]$, 7/15 moles of ferro-magnesian exchange component $[Fe_1Mg_{-1}]$, and -4/15 moles of soda-potassic exchange component $[Na_1K_{-1}]$ (Thompson, 1982; Burt, 1989, 1994). This produces tourmaline composition $[K_{4/15}Na_{1/15}Mg_{28/15}Fe_{7/15}Al_{20/3}Si_6(BO_3)_3O_{18}(OH)_4]$ with a Mg-foitite affinity (Adlakha and Hattori, 2016).

Unfortunately, high sample densities do not occur at other points on Figures 32 to 35 that possibly correspond to other mineral compositions. Nevertheless, the existence of other minerals can be deduced using the data trends observed on these diagrams. For example, on Figure 32, high sample densities occur on a line between the Mg-phengitic illite node (0.30,0.05) and the origin, and between the Mg-foititic tourmaline node and the origin, suggesting that a mineral plots at (or near) the origin. This

mineral is likely kaolin [kaolinite, dickite, halloysite: $Al_4Si_4O_{10}(OH)_8.4H_2O$, or nacrite: $Al_2Si_2O_5(OH)_4$]. Similarly, high sample densities occur along a line with steep negative slope that passes through the Mg-foititic tourmaline node. Although this data trend is too diffuse to deduce the exact composition of this mineral, it is likely sudoite, which has an ideal composition of $Mg_4Al_8Si_6O_{20}(OH)_{16}$, as sudoite has been recognized in Athabasca sandstones associated with unconformity U deposits by Scott et al. (2012), Dann et al. (2012) and Alexandre et al. (2005). In the 4604 sample lithogeochemical dataset, SiO_2 concentrations were not analyzed. Consequently, in the following data analysis, proxy SiO_2 concentrations were calculated by difference (100% minus the sum of all major oxides), after deducing how much H_2O was present in illite, tourmaline, kaolin and sudoite, and how much BO_3 was present in tourmaline, using the appropriate H_2O- and BO_3-to-K_2O, -Na_2O, -MgO and -Al_2O_3 mass ratios for these minerals.

Using the mineral compositions deduced from the GER diagrams in Figures 32 to 35, as well as additional minerals in these rocks identified by other workers (Scott et al., 2012; Dann et al., 2012; Alexandre et al., 2005), an essential mineral suite for Manitou Falls Formation rocks above the Phoenix unconformity U deposit was identified for the change of basis calculation (Stanley, 2017). It consists of: quartz (QRTZ), (Mg-phengitic) illite (ILLT), kaolin (KAOL), (Mg-foititic) tourmaline (FOIT), sudoite (SUDO), apatite (APAT), crandallite (CRAN), hematite (HEMA) and rutile (RUTL). The corresponding mineral compositions were placed in a *C* matrix (Equation E11) and inverted to allow calculation of the modes of these essential minerals using the lithogeochemical data (with the SiO_2 proxy) via the change of basis classification procedure (Stanley, 2017). Results illustrate vertical mineralogical zoning likely controlled by Athabasca Basin stratigraphy (deposition and diagenesis), and Phoenix deposit hydrothermal alteration (Figures 36, 37, and 38).

$$C = \begin{array}{c} \\ QRTZ \\ KAOL \\ SUDO \\ ILLT \\ APAT \\ HEMA \\ FOIT \\ CRAN \\ RUTL \end{array} \begin{array}{ccccccccc} Si & Al & Ca & Fe & K & Mg & Na & P & Ti \\ \begin{bmatrix} 1 & 0 & 0 & 0 & 0 & 0 & 0 & 0 & 0 \\ 2 & 2 & 0 & 0 & 0 & 0 & 0 & 0 & 0 \\ 6 & 8 & 0 & 0 & 0 & 4 & 0 & 0 & 0 \\ 27/4 & 5 & 0 & 0 & 59/40 & 1/4 & 1/40 & 0 & 0 \\ 0 & 0 & 5 & 0 & 0 & 0 & 0 & 3 & 0 \\ 0 & 0 & 0 & 2 & 0 & 0 & 0 & 0 & 0 \\ 6 & 20/3 & 0 & 7/15 & 4/15 & 28/15 & 1/15 & 0 & 0 \\ 0 & 3 & 1 & 0 & 0 & 0 & 0 & 2 & 0 \\ 0 & 0 & 0 & 0 & 0 & 0 & 0 & 0 & 1 \end{bmatrix} \end{array} \qquad \text{(E11)}$$

Figure 36 illustrates that overall very high quartz concentrations occur in the Read and Manitou Falls formations. This suggests that these sediments were very chemically mature or were transported large distances. Lower quartz concentrations in the B and C members may be due to 'closure' (Aitchison, 1986), whereby an abundance of clay and alteration minerals (illite, kaolinite, tourmaline, and sudoite) merely dilutes the quartz to lower concentrations. These other minerals may be present in that part of the stratigraphy because of changing source terrane compositional variations, diagenetic effects, or hydrothermal alteration from the subjacent Phoenix unconformity U deposit.
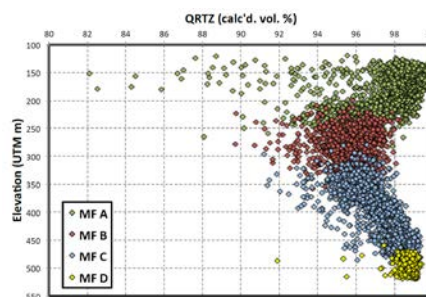

Figure 36: Scatterplot of the calculated quartz modes plotted against depth in near-vertical drill-cores through the Phoenix unconformity U deposit, Saskatchewan (n = 4604).

Figure 37 presents the mineral modes of the major minerals, other than quartz, in the Read and Manitou Falls formations. Illite is abundant in Members B and C, possibly due to higher concentrations of mudstones in the sequence, or due to distal hanging wall alteration. Tourmaline exhibits a 'striped' pattern because its modal calculation involves a relatively large coefficient for Na, and which has very low Na_2O concentrations relative to its 0.01% reporting interval. This produces a mathematically induced 'striped' pattern.
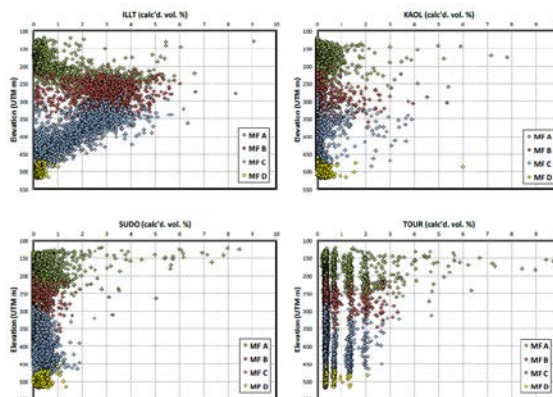

Figure 37: Scatterplot of the calculated minor mineral modes (illite: upper left; kaolin: upper right; sudoite: lower left; tourmaline: lower right) plotted against depth in near-vertical drill-cores through the Phoenix unconformity U deposit, Saskatchewan (n = 4604).

Figure 38 presents the mineral modes of the minor minerals in the Read and Manitou Falls formations. Hematite and rutile (leucoxene?) exhibit marginally higher concentrations in Members B and C, and crandallite exhibits higher concentrations in the top half of Member B, and Members C and D.

Lastly, a stacked histogram of mineral modes in the discovery drill-core for the Phoenix unconformity U deposit (WR-249) is presented in Figure 39, and mimics the patterns observed in Figures 36, 37 and 38.
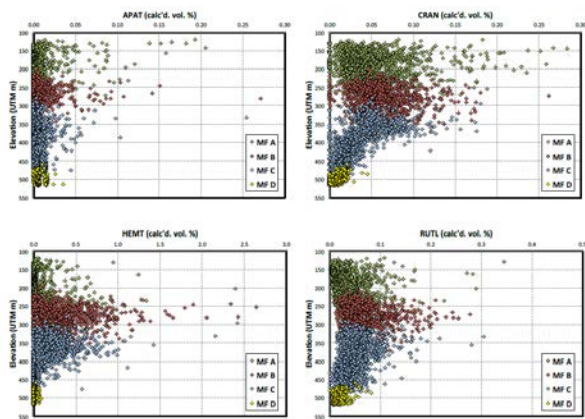
Figure 38: Scatterplot of the calculated trace mineral modes (apatite: upper left; crandallite: upper right; hematite: lower left; rutile: lower right) plotted against depth in near-vertical drill-cores through the Phoenix unconformity U deposit, Saskatchewan (n = 4604).
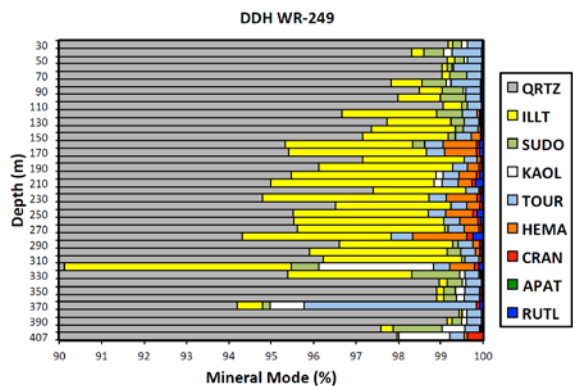

Figure 39: Scatterplot of the calculated quartz modes plotted against depth in discovery DDH WR-249 through the Phoenix unconformity U deposit, Saskatchewan (n = 40).

In summary, MER analysis of this substantial sedimentary rock lithogeochemical dataset has revealed a number of interesting features in the data with significant mineralogical and petrological implications. Mineral modes calculated from the lithogeochemical data have significant utility in that they can be used to quantitatively develop alteration models for mineralization, as well as document facies variations and diagenetic effects that have influenced sedimentary rocks in the Athabasca Basin. Both of these features provide important information to geoscientists, allowing them to better explore for unconformity U deposits in the Athabasca Basin.

East Kemptville Sn Greisen Deposit, Nova Scotia

The East Kemptville Sn greisen deposit is hosted by leucogranites of the Davis Lake Pluton, South Mountain Batholith. It is located 25 km northwest of Yarmouth, Nova Scotia, and was discovered in 1978 and mined by open pit methods between 1985 and 1992 by Rio Algom Ltd. Recently, Avalon Advanced Materials Inc. has been re-evaluating the

deposit to determine whether the mine can be re-opened within the current economic climate.

The deposit occurs at the top of a muscovite-bearing leucomonzogranite that hosts structurally controlled 'regional' greisens with disseminated Sn-Cu-Zn mineralization cut by 'zoned' greisen veins (Richardson, 1988; Kontak, 1990; Halter et al., 1995, 1996). Hydrothermal alteration consists of distal muscovite and proximal topaz in both styles of mineralization.

In 2014 and 2015, Avalon drilled 29 holes to confirm grades and obtain a modern understanding of the deposit geology. Logging was accompanied by lithogeochemical sampling, analysis (fusion/ICP) and MER data evaluation to assist with the logging and resulting geological interpretations. In the following MER data evaluation, only samples from the 2014 diamond drilling program (n = 373) were evaluated, as Zr was not analyzed in the 2015 samples.

Conserved element analysis revealed the existence of three distinct leucogranite compositions recognizable using Th, La, Zr and Y ratios, among others (Figure 40).
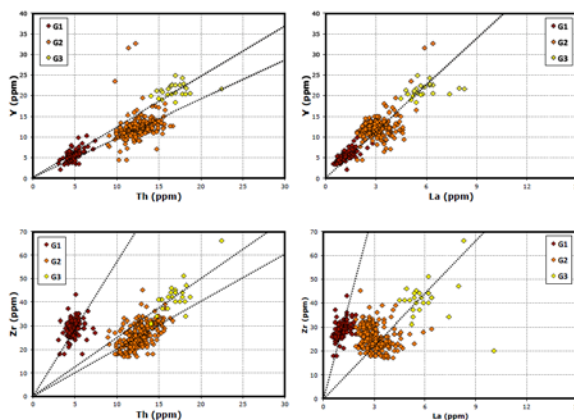

Figure 40: Conserved element scatterplots with Th and La on the x-axes and Zr and Y on the y-axes for granitoid rocks from the East Kemptville Sn greisen deposit, Nova Scotia.

These three leucomonzogranite compositions are spatially consistent and vertically stacked (Figures 41, 42), with small dykes adjacent to their contacts. Furthermore, these granite compositions define a fractionation sequence whereby the innermost (deepest) granite (G3) is the most fractionated (exhibiting the highest conserved element concentrations). Lastly, the cross-sections in Figures 41 and 42 suggest that the Baby Zone may be uplifted relative to the Main Zone, and this could explain why there are higher grades and hydrothermal breccia bodies in the (possibly deeper) Baby Zone.

Using Zr as a conserved element, samples were plotted on a PER diagram testing the hypothesis of feldspar fractionation to understand their compositional diversity (Figure 43).

Because fresh granite samples contain both alkali feldspar and igneous muscovite, and biotite is largely absent, they plot on the

dark blue dashed line of Figure 43. In contrast, hydrothermally altered samples contain additional hydrothermal muscovite and topaz, and so plot below this line. Hydrothermal alteration at East Kemptville appears to take three different forms: muscovite alteration of alkali feldspar (green arrow; Figure 43), topaz alteration of muscovite (light blue arrow; Figure 43), and a third alteration style involving Al addition and producing additional topaz (brown arrow; Figure 43). Because of their vertical trends, the first two hydrothermal alteration reactions can be balanced on Al.
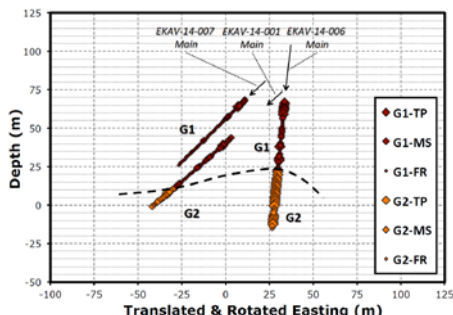

Figure 41: Oblique cross section depicting 2014 drill-core samples looking NE through the Main Zone of the East Kemptville Sn greisen deposit, Nova Scotia. Symbol sizes reflect alteration zones, as described.
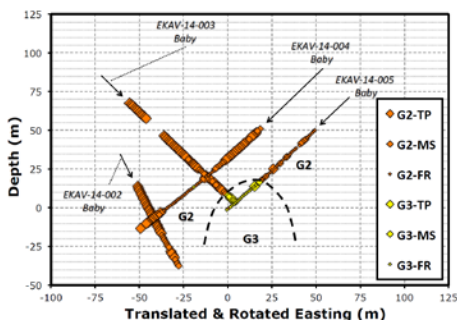

Figure 42: Oblique cross section depicting 2014 drill-core samples looking NE through the Baby Zone of the East Kemptville Sn greisen deposit, Nova Scotia.
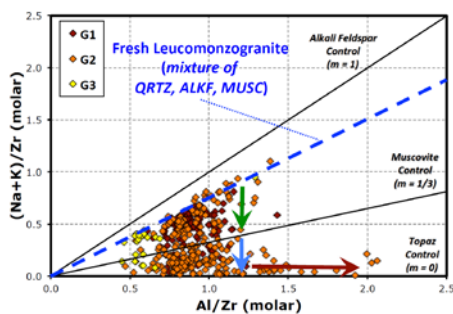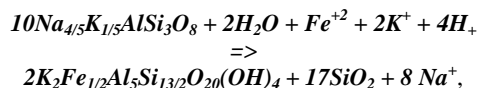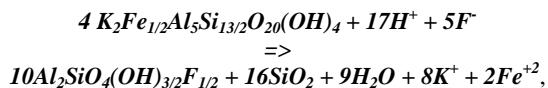

Figure 43: PER diagram plotting Al/Zr versus (Na+K)/Zr tests a feldspar fractionation hypothesis for granitoid rocks from the East Kemptville Sn greisen deposit, Nova Scotia.
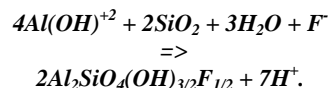
Other PER diagrams indicate that the bulk composition of the two feldspars in these rocks (albite and K-feldspar) is OR_{20}. Additionally, electron microprobe and MER analysis indicate that hydrothermal muscovite in this deposit is Fe-phengite with an approximate composition of $[K_2Fe_{1/2}Al_5Si_{13/2}O_{20}(OH)_4]$. Lastly, electron microprobe results indicate that the topaz has an approximate composition of $[Al_2SiO_4(OH)_{3/2}F_{1/2}]$. These constraints, along with Al addition for the third reaction, allow balancing of the three geochemical reactions responsible for muscovite alteration of alkali feldspar (+ quartz):

$$10Na_{4/5}K_{1/5}AlSi_3O_8 + 2H_2O + Fe^{+2} + 2K^+ + 4H_+$$
$$=>$$
$$2K_2Fe_{1/2}Al_5Si_{13/2}O_{20}(OH)_4 + 17SiO_2 + 8\,Na^+,$$

topaz alteration of muscovite (+ quartz):

$$4\,K_2Fe_{1/2}Al_5Si_{13/2}O_{20}(OH)_4 + 17H^+ + 5F^-$$
$$=>$$
$$10Al_2SiO_4(OH)_{3/2}F_{1/2} + 16SiO_2 + 9H_2O + 8K^+ + 2Fe^{+2},$$

and topaz alteration of quartz:

$$4Al(OH)^{+2} + 2SiO_2 + 3H_2O + F^-$$
$$=>$$
$$2Al_2SiO_4(OH)_{3/2}F_{1/2} + 7H^+.$$

The volume changes associated with these three alteration reactions are -5%, -27% and +111%, respectively. As a result, the first two reactions are self-perpetuating, and likely to produce widespread alteration zones, whereas the third reaction is self-limiting and likely to produce spatially restricted alteration zones. In fact, all three styles of alteration can be recognized, in order, in 'zoned' greisens adjacent to cassiterite veins in the deposit (Figure 44).
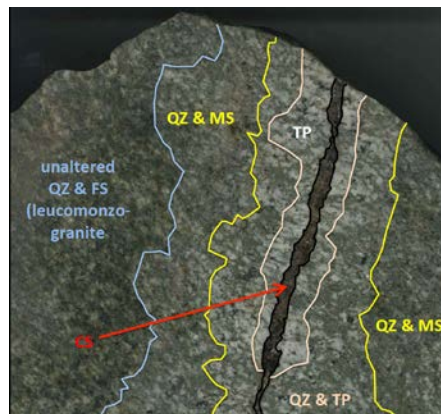
Figure 44: Photograph of 20 cm wide slab cut by a cassiterite vein (CS) from the East Kemptville Sn greisen deposit, Nova Scotia. The vein exhibits three alteration envelopes: muscovite+quartz, topaz+quartz, and topaz-only.

Given an understanding of the styles of alteration present at East Kemptville, controls on mineralization of various types can be assessed using the PER diagram bubbleplots presented in Figure 45. High concentrations of Sn (cassiterite) appear to occur in all three alteration zones, whereas high Cu (chalcopyrite) and Zn (sphalerite) concentrations are found within topaz+quartz

alteration zones. Lastly, modest but anomalous concentrations of W (scheelite) occur in rocks containing only topaz (no muscovite or alkali feldspar). Consequently, the alteration and mineralization zoning at East Kemptville appear to be coupled.

A possible explanation for at least some of this zoning is the Fe liberated from phengite during the muscovite-to-topaz+quartz reaction. This Fe could have caused the saturation of both chalcopyrite and the Fe-rich sphalerite found at East Kemptville, forcing these minerals to co-precipitate in the topaz+quartz alteration zone. Because Fe was consumed during the alkali feldspar-to-muscovite+quartz reaction, these same minerals would be unlikely to saturate during this first alteration style.
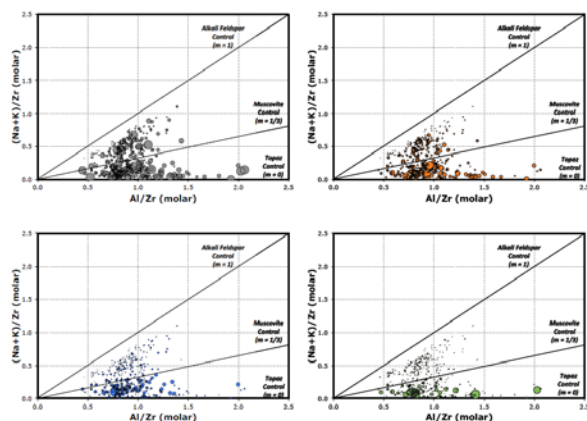

Figure 45: PER bubbleplot diagrams identical to Figure 43 with bubble diameters corresponding to Sn (upper left), Cu (upper right), Zn (lower left) and W (lower right) concentrations for granitoid rocks from the East Kemptville Sn greisen deposit, Nova Scotia.

Because cassiterite doesn't have Fe in its formula, its stability is not subject to such controls, and it likely precipitated for reasons that would be ubiquitous across all three alteration zones (e.g., due to cooling, or an increase in pH - at least for the first two reactions (Halter et al., 1995)).

Lastly, scheelite precipitation is difficult to explain, as the host rocks have very low Ca concentrations (averaging 0.52 wt. % CaO in fresh leucomonzogranite). As a result, other Ca-bearing minerals, such as fluorite or apatite, likely competed for Ca with scheelite, and if present, these minerals would limit scheelite precipitation. However, the F necessary for the precipitation of topaz may be derived from the destruction of earlier formed apatite or fluorite, a process that would liberate Ca. As a result, the formation of topaz and precipitation of scheelite could be linked.

A change of basis calculation (Stanley, 2017) was undertaken using the rocks from East Kemptville to provide mineralogical variables for examination. The essential mineral assemblage in the East Kemptville leucomonzogranites consists of quartz (QRTZ), alkali feldspar (OR_{20}; ALKF), muscovite (Fe-phengite; MUSC), topaz (TOPZ), apatite (APAT), fluorite (FLRT), pyrrhotite (PYRH), chalcopyrite (CHPY), sphalerite (SPHL) and cassiterite (CASS). The compositions of these minerals were placed in a *C* matrix (Equation E12) and inverted, and the

calculations necessary to produce modal abundances of these essential minerals were then undertaken.

Results have been used in a variety of ways. Down-hole plots of mineral modes reflect the alteration zoning described previously (Figure 46). Unfortunately, such data cannot be used to recognize the smaller-scale 'zoned' greisens (Figure 44), as these tend to be smaller than the size of the sample intervals (1.5 m). This explains why a ternary diagram plotting alkali feldspar, muscovite and topaz (Figure 47) doesn't illustrate the sequential alteration from fresh feldspar to muscovite to topaz, as the sample intervals are too large to resolve all three alteration styles from a single zoned greisen.

$$
C = \begin{array}{c} \\ QRTZ \\ ALKF \\ MUSC \\ TOPZ \\ APAT \\ FLRT \\ PYRH \\ SPHL \\ CHPY \\ CASS \end{array}
\begin{array}{ccccccccccc}
Si & Al & Na & K & Ca & P & Fe & Zn & Cu & Sn \\
1 & 0 & 0 & 0 & 0 & 0 & 0 & 0 & 0 & 0 \\
3 & 1 & 4/5 & 1/5 & 0 & 0 & 0 & 0 & 0 & 0 \\
13/4 & 5/2 & 0 & 1 & 0 & 0 & 1/4 & 0 & 0 & 0 \\
1 & 2 & 0 & 0 & 0 & 0 & 0 & 0 & 0 & 0 \\
0 & 0 & 0 & 0 & 5 & 3 & 0 & 0 & 0 & 0 \\
0 & 0 & 0 & 0 & 1 & 0 & 0 & 0 & 0 & 0 \\
0 & 0 & 0 & 0 & 0 & 0 & 1 & 0 & 0 & 0 \\
0 & 0 & 0 & 0 & 0 & 0 & 0 & 1 & 0 & 0 \\
0 & 0 & 0 & 0 & 0 & 0 & 1 & 0 & 1 & 0 \\
0 & 0 & 0 & 0 & 0 & 0 & 0 & 0 & 0 & 1
\end{array} \quad (E12)
$$

Another application of these calculated mineral modes is the prediction of rock properties, which in many cases are simply weighted averages of the corresponding mineral properties. Thus, given knowledge of the proportion of each mineral, the corresponding rock property can be calculated. As a result, lithogeochemical data is able to tangibly contribute to the ore body knowledge necessary for deposit evaluation, mine planning, mining and remediation by allowing prediction of rock properties germane to these activities.
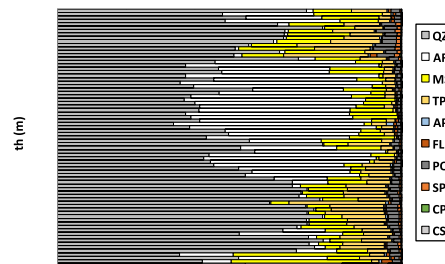
Figure 46: Down hole calculated mineral modes from DDH EKAV-14-004 quantitatively identify relatively fresh G2 leucomonzogranite (between 100–150 m) surrounded by more intensely altered muscovite- and topaz-bearing zones.

For example, the bulk density of a rock is equal to the weighted mean of the densities of the minerals within the rock, provided that the porosity is negligible:

$$ \hat{\rho}_{ROCK} = \sum_{i=1}^{n} x_{MIN_i} \rho_{MIN_i}. \quad (E13) $$

Using the ideal densities for the essential minerals in the East Kemptville rocks, estimates of the bulk rock densities of the 1.5 m long half core lithogeochemical samples were determined using Equation E13 and were plotted against 183 measured

densities of 15 cm long whole core samples from within these intervals. Results presented on Figure 48 indicate that the calculated bulk rock densities over-estimate the measured densities, likely because the lithogeochemically-derived values do not accommodate rock porosity. Furthermore, the degree of over-estimation varies substantially, indicating that porosity is likely not a constant. Lastly, the poor correlation observed (0.59) in Figure 48 is likely not solely a function of porosity, but also a function of the different sample supports (Sinclair and Blackwell, 2006), as their shapes are different and their masses differ by a factor of 5.
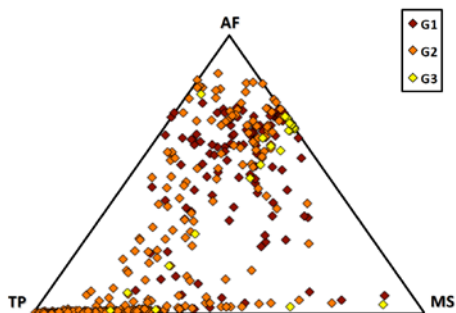

Figure 47: Ternary diagram of calculated alkali feldspar, muscovite and topaz volume mineral modes from the East Kemptville Sn greisen vein deposit, Nova Scotia. The alteration trend does not pass through the muscovite vertex, as these 1.5 m long samples commonly include mixtures of fresh, muscovite-altered and topaz-altered rocks from small-scale 'zoned' greisens.
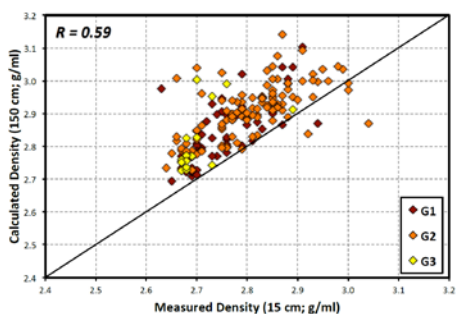

Figure 48: Scatterplot of 201 measured bulk rock densities from 15 cm long whole core samples plotted against the corresponding calculated bulk rock densities from lithogeochemical data collected from 1.5 m long half core samples of leucomonzogranites from the East Kemptville Sn greisen deposit, Nova Scotia.

To address this issue, 89 representative bulk rock density measurements were collected from 1.5 m long, quarter core intervals corresponding to existing lithogeochemical samples and spanning the range of densities observed in the 15 cm whole core measurements. The calculated mineral modes were then regressed against these density measurements using an objective function analogous to Equation E13:

$$\hat{\rho}_{ROCK} = \sum_{i=1}^{n} x_{MIN_i} \beta_i. \qquad \text{(E14)}$$

Ideally, in the absence of porosity, analytical error, non-essential minerals and mineral composition variations, the regression parameters (βs) should approximate the associated mineral densities. Unfortunately, all of these factors do exist, so the βs do not closely approximate the ideal mineral densities. Nevertheless, results provide a regression equation that accurately predicts rock density from the lithogeochemical data (Figure 49). The high correlation associated with these regression results (0.96) indicates that reliable bulk rock densities can be obtained from lithogeochemical data, provided that an accurate essential mineral suite and essential mineral compositions can be identified. As a result, if lithogeochemical data were collected during ore definition drilling, numerous density estimates could be obtained, after calibration with a modest number of actual measurements, at no incremental cost, allowing the development of a block model for rock density during resource assessment.
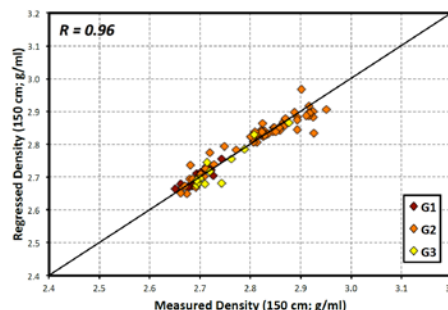

Figure 49: Scatterplot of 89 measured bulk rock densities from 1.5 m long whole core samples plotted against regressed bulk rock density estimates from lithogeochemical data collected from 1.5 m long quarter core samples of leucomonzogranites from the East Kemptville Sn greisen deposit, Nova Scotia.

DISCUSSION AND CONCLUSIONS

The five case histories presented above illustrate how lithogeochemical data, evaluated using MER methods, can be used to assist in a large number of mineral exploration- and mining-related activities. These case histories represent a diverse set of geological environments and mineral deposit types, illustrating the adaptability of MER analysis to a wide range of problems that can be solved by lithogeochemical means. Consequently, it is likely that additional challenges encountered in mineral exploration and mining can be addressed using similar strategies.

Examples where lithogeochemistry has made important contributions range from routine geological mapping and drill-core logging, to understanding alteration reactions and zoning (including assemblage, order and spatial extent) and ore mineral precipitation controls, as well as the prediction of rock properties. This last aspect is likely to offer significant opportunity in the future, especially if mining companies continue collecting whole rock lithogeochemical data during exploration to assist mapping and drill-core logging. Thus, using

lithogeochemical analysis and MER data evaluation as validation for drill-core logging results, which represents on the order of 2 to 5% of drilling costs, could provide important dataset legacies to later resource evaluation, mine planning, mining and mine remediation.

At East Kemptville, rock densities can be reliably predicted using volume mineral modes calculated from lithogeochemical data collected routinely during exploration. However, there is no reason that other rock properties cannot also be predicted from these calculated mineral modes. Possible rock properties that could also be predicted include:

- *Hardness*: as it relates to finer-grain size (secondary) crusher performance;
- *Neutralizing potential*: as a control on tailings water treatment;
- *Magnetic susceptibility*: for future geophysical exploration and interpretation; and
- *Phyllosilicate concentration*: as a possible cause for degradation of flotation performance.

Furthermore, it is also possible that the difference between lithogeochemically calculated rock densities (as presented on the vertical axis of Figure 48) and measured rock densities could provide reliable estimates of rock porosity. In all cases, the only costs of these estimates would be that of calculation, as no additional measurements would be required to determine these rock properties (save porosity), once the proper lithogeochemical data has been collected and evaluated.

Consequently, exciting advances in data analysis, and in particular molar element ratio analysis, of lithogeochemical data provide significant advantage to mineral explorationists and mining engineers/geologists in today's resource environment. These advantages can only be achieved if proper and systematic collection and analysis of lithogeochemical data are undertaken during drilling, so that the data are available later in the exploration cycle, when the measurement of a diverse range of rock properties is required.

REFERENCES

Adlakha, E.E. and K. Hattori, 2016, Paragenesis and composition of tourmaline types along the P2 fault and McArthur River uranium deposit, Athabasca Basin, Canada: Canadian Mineralogist, 54, 661-679.

Aitchison, J., 1986, The Statistical Analysis of Compositional Data, Monographs on Statistics and Applied Probability: Chapman and Hall.

Alenius, E.M.J., 1968, A brief history of the United Verde open pit, Jerome, Arizona: Arizona Bureau of Mines, 178, 34 p.

Alexandre, P., K. Kyser, P. Polito, and D. Thomas, 2005, Alteration mineralogy and stable isotope geochemistry of Paleoproterozoic basement-hosted unconformity-type uranium deposits in the Athabasca Basin, Canada: Economic Geology, 100 (8), 1547-1563.

Anderson, C.A. and S.C. Creasey, 1958, Geology and ore deposits of the Jerome area, Yavapai County, Arizona: U.S. Geological Survey, Professional Paper, 308, 185 p.

Benavides, J., T.K. Kyser, A.H. Clark, C.R. Stanley, and C. Oates, 2008a, Exploration guidelines for copper-rich iron oxide-copper-gold deposits using molar element ratio analysis and oxygen isotopes, Mantoverde area, northern Chile: the integration of host-rock element ratios and oxygen isotope compositions: Geochemistry: Exploration, Environment, Analysis, 8 (3-4), 343-367.

Benavides, J., T.K. Kyser, A.H. Clark, C.R. Stanley, and C. Oates, 2008b, Application of molar element ratio analysis of lag talus composite samples to the exploration for iron oxide-copper-gold mineralization: Mantoverde area, northern Chile: Geochemistry: Exploration, Environment, Analysis, 8 (3-4), 369-380.

Bettaney, L. and C.R. Stanley, 2001, Geochemical data quality: The "fit-for-purpose" approach: EXPLORE: Newsletter of the Association of Exploration Geochemists, 111, 12-22.

Bevins, R. E., B.P. Kokelaar, and P.N. Dunkley, 1984, Petrology and geochemistry for lower to middle Ordovician igneous rocks in Wales: A volcanic arc to marginal basin transition: Proceedings of the Geologists' Association, 95, 337–347.

Burt, D.M., 1988, Vector representation of phyllosilicate compositions: Reviews in Mineralogy, 19, 561-599.

Burt, D.M., 1989, Vector representation of tourmaline compositions: American Mineralogist, 74, 826.

Burt, D.M., 1994, Exchange vector diagrams for the compositions of alteration minerals: Geological Association of Canada, Short Course Notes, 11, 31 p.

Byers, A.R., 1957, Geology and mineral deposits of the Hanson Lake area, Saskatchewan: Saskatchewan Geological Survey, Report 30, 1-47.

Chen, S., K. Hattori, E. Grunsky, and Y. Liu, 2015, Geomathematical study of sandstones overlying the Phoenix uranium deposits and the REE-rich Maw Zone, Athabasca Basin, Saskatchewan, in E.G. Potter and D.M. Wright, eds., Targeted Geoscience Initiative 4: Unconformity-related Uranium Systems, Geological Survey of Canada, Open File 7791, 21-31.

Coleman, L.C., J.W. Gaskarth, and J.R. Smith, 1970, Geology and geochemistry of the Hanson Lake area, Saskatchewan: Saskatchewan Research Council, Geological Division Report 10, 156 p.

Dann, J., K. Hattori, and C. Sorba, 2012, Alteration minerals and elemental assemblages around the Phoenix uranium deposit, Athabasca Basin, Saskatchewan: 2012 Joint Annual Meeting, Expanded Abstracts, Geological Association of Canada and Mineralogical Association of Canada.

Gaskarth, J.W., 1967, Petrogenesis of Precambrian rocks in the

Hanson Lake area, east-central Saskatchewan: PhD thesis, University of Saskatchewan.

Gustin, M.S., 1988, A petrographic, geochemical, and stable isotope study of the United Verde ore body and it associated alteration, Jerome, Arizona: PhD thesis, University of Arizona.

Gustin, M.S., 1990, Stratigraphy and alteration of the host rocks, United Verde massive sulfide deposit, Jerome, Arizona: Economic Geology, 85, 29-49.

Halter, W.E., A.E. Williams-Jones, and D.J. Kontak, 1996, The role of greisenization in cassiterite precipitation at the East Kemptville tin deposit, Nova Scotia: Economic Geology, 91, 368-385.

Halter, W.E., A.E. Williams-Jones, and D.J. Kontak, 1995, Origin and evolution of the greisenizing fluid at the East Kemptville tin deposit, Nova Scotia, Canada: Economic Geology, 93, 1026-1051.

Hiatt, E.E. and T.K. Kyser, 2005, Sequence stratigraphy, hydrostratigraphy, and mineralizing fluid flow in the Proterozoic Manitou Falls Formation, eastern Athabasca Basin, Saskatchewan, in C.W. Jefferson and G. Delaney, eds., EXTECH IV: Geology and Uranium EXploration TECHnology of the Proterozoic Athabasca Basin, Saskatchewan and Alberta: Geological Survey of Canada, Bulletin 588, 1-22.

Jenkins, R., 2012, X-Ray Fluorescence Spectrometry: John Wiley & Sons.

Kontak, D.J., 1990, The East Kemptville topaz-muscovite leucogranite, Nova Scotia; 1: Geological setting and whole-rock geochemistry: Canadian Mineralogist, 28, 787-825.

Koziol, M., 1985, Hanson Lake project, Summary of 1985 field activities, Internal Company Report, NTS 63L/10: Saskatchewan Mining Development Corporation & Esso Minerals Joint Venture, 147 p.

Koziol, M. and W. Stoeterau, 1984, Hanson Lake project, Summary of 1984 field activities, Internal Company Report, NTS 63L/10: Saskatchewan Mining Development Corporation, 74 p.

Koziol, M. and G. Ostapovitich, 1993, The McIlvenna Bay massive sulphide deposit – A case history: Saskatchewan Geological Survey, Modern Exploration Techniques, 54-70.

Kramar, S., 2017, Lithostratigraphy of the Hanson Lake assemblage, Flin Flon greenstone belt, Saskatchewan, Canada: MSc thesis, Acadia University.

Kreczmer, M. and R. Koch, 1983, Hanson Lake Project, Summary of 1983 Field Activities, Internal Company Report, NTS 63L/10: Saskatchewan Mining Development Corporation, 109 p.

Madeisky, H.E. and C.R. Stanley, 1993, Lithogeochemical exploration for metasomatic zones associated with volcanic-

hosted massive sulphide deposits using Pearce element ratio analysis: International Geological Reviews, 35, 1121-1148.

Maxeiner, R. O., T.I.I. Sibbald, and B.R. Watters, 1993, Geology of the Hanson Lake area (Part of NTS 63L-10): Saskatchewan Geological Survey, Summary of Investigations, 93-4, 40-49.

Maxeiner, R.O., T.I.I. Sibbald, J.F. Lewry, and B.R. Watters, 1995, Geology of the Deschambault-Tulabi-Hanson Lakes area, southern Hanson Lake Block, northern Saskatchewan (Part of NTS 63L/10,11,14,15): Geological Survey of Canada, Open File 3218, 1-137.

Maxeiner, R.O., T.I. Sibbald, W.L. Slimmon, L.M. Heaman, and B.R. Watters, 1999, Lithogeochemistry of volcano-plutonic assemblages of the southern Hanson Lake Block and southeastern Glennie Domain, Trans-Hudson Orogen: Evidence for a single island arc complex: Canadian Journal of Earth Sciences, 36, 209–225.

Meschede, M., 1986, A method of discriminating between different types of mid-ocean ridge basalts and continental tholeiites with the Nb-Zr-Y diagram: Chemical Geology, 56, 207-218.

Miller, J.D., 2011, Field trip 1: Igneous stratigraphy of the layered series at Duluth; Type intrusion of the Duluth Complex: Institute on Lake Superior Geology, Proceedings and Abstracts, 57, 3-29.

Mireku, L.K. and C.R. Stanley, 2007, Lithogeochemistry and hydrothermal alteration at the Halfmile Lake South Deep zone, a volcanic-hosted massive sulphide deposit, Bathurst mining camp, New Brunswick: Exploration and Mining Geology, 15, 177-199.

Morelli, R.M., 2012, Regional data compilation and three-dimensional geological modelling in the vicinity of the Shield margin, Hanson Lake area, in Summary of Investigations 2012, Volume 2, Saskatchewan Geological Survey, Saskatchewan Ministry of the Economy, Miscellaneous Report 2012-4.2, Paper A-8, 12 p.

Morelli, R.M. and R.O. Maxeiner, 2014, Geochemical data compilation of the Hanson Lake assemblage and sub-Phanerozoic extensions: Proposed implications for tectonic setting and volcanogenic massive sulphide mineralization: Saskatchewan Ministry of the Economy, Saskatchewan Geological Survey, Open File Report, 2013-2, 25 p.

Murphy, D.M.K. and C.R. Stanley, 2007, Lithogeochemical constraints on the host rock, hydrothermal alteration and weathering of the Groundrush gold deposit: Geochemistry: Exploration, Environment, Analysis, 7, 363-375.

Nicholls J., 1988, The statistics of Pearce element diagrams and the Chayes closure problem: Contributions to Mineralogy and Petrology, 99, 36-43.

Nicholls, J. and T.M. Gordon, 1994, Procedures for the

calculation of axial ratios on Pearce element ratio diagrams: Canadian Mineralogist, 32, 969-977.

O'Connor-Parsons, T. and C.R. Stanley, 2007, Downhole lithogeochemical patterns relating to chemostratigraphy and igneous fractionation processes in the Golden Mile dolerite, Western Australia: Geochemistry: Exploration, Environment, Analysis, 7, 109-127.

Parslow, G.R. and J.W. Gaskarth, 1986, Geochemistry of the Hanson Lake area, Summary of Investigations: Saskatchewan Energy and Mines, Open File, 86-1, 106 p.

Pearce, T.H., 1968, A contribution to the theory of variation diagrams: Contributions to Mineralogy and Petrology, 19, 142-157.

Pearce, J.A., 1996, A user's guide to basalt discrimination diagrams, in D.A. Wyman, ed., Trace Element Geochemistry for Volcanic Rocks; Applications for Massive Sulphide Exploration: Short Course Notes, Geological Association of Canada, 12, 79-113.

Polito, P.A., T.K. Kyser, and C.R. Stanley, 2009, Origin and evolution of the Proterozoic Valhalla uranium deposit, Queensland, Australia: Mineralium Deposita, 44, 11-40.

Polito, P.A., T.K. Kyser, P. Alexandre, E.E. Hiatt, and C.R. Stanley, 2011, Advances in understanding the Kombolgie Subgroup and unconformity-related uranium deposits in the Alligator Rivers Uranium Field and how to explore for them using lithogeochemical principles: Australian Journal of Earth Sciences, 58, 453-474.

Ramaekers, P., 1979, Sections through the Athabasca Basin, Summary of Investigations 1979: Saskatchewan Geological Survey, Saskatchewan Department of Mineral Resources, Miscellaneous Report 79-10.

Ramaekers, P., 1980, Stratigraphy and tectonic history of the Athabasca Group (Helikian) of northern Saskatchewan: Saskatchewan Geological Survey, Summary of Investigations 1980, 99–106.

Ramaekers, P., 1990, Geology of the Athabasca Group (Helikian) in northern Saskatchewan: Saskatchewan Geological Survey, Geological Report 195, 49 p.

Richardson, J.M., 1988, Genesis of the East Kemptville greisen-hosted tin deposit, Davis Lake Complex, southwestern Nova Scotia, Canada: PhD thesis, Carleton University.

Robinson, M., C.I. Godwin, and C.R. Stanley, 1996, Geology, lithogeochemistry and alteration of the Battle volcanogenic massive sulphide zone, Buttle Lake mining camp, Vancouver Island, British Columbia: Economic Geology, 91, 527-548.

Roscoe, W.E., 2014, Technical report on a mineral resource estimate update for the Phoenix uranium deposit, Wheeler River project, Athabasca Basin, Saskatchewan (43-101 Report): RPA Inc.

Russell, J.K. and C.R. Stanley, 1990, A theoretical basis for the development and use of chemical variation diagrams: Geochimica et Cosmochimica Acta, 5, 2419-2431.

Scott, R., G. Chi, and S. Bosman, 2012, Petrographic characteristics of the Athabasca Group sandstones from the Rumpel Lake drill core, Athabasca Basin, northern Saskatchewan, in Summary of Investigations 2012, Vol. 2: Saskatchewan Geological Survey, Saskatchewan Ministry of the Economy, Miscellaneous Report 2012-4.2, Paper A-7, 8p.

Severson, M.J. and S.A. Hauck, 2008, Finish logging of Duluth Complex drill core (And a reinterpretation of the geology at the Mesaba (Babbitt) deposit): Natural Resources Research Institute, University of Minnesota, Duluth, Technical Report NRRI/TR-2008/17, 68p.

Shervais, J.W., 1982, Ti-V plots and the petrogenesis of modern and ophiolitic lavas: Earth and Planetary Science Letters, 59, 101-118.

Sibbald, T.I.I., 1989, Base metal deposits and geology of the Early Proterozoic Hanson Lake metavolcanics, in Summary of Investigations 1989, Saskatchewan Geological Survey, Saskatchewan Energy and Mines, Miscellaneous Report 89-4, 66-70.

Sinclair, A.J. and G.H. Blackwell, 2006, Applied Mineral Inventory Estimation: Cambridge University Press.

Smith, W.F. and J. Hashemi, 2006, Foundations of Materials Science and Engineering (4th ed.): McGraw-Hill, 318–320.

Sopuck, V. and B. Duncan, 1990, 1990 Hanson Lake project lithogeochemistry compilation: Cameco Corporation Internal Report, 3 Volumes, 693 p.

Stanley, C.R., 1998, Lithogeochemical exploration for metasomatic zones associated with hydrothermal mineral deposits using molar element ratio analysis: Advanced topics, Lithogeochemical Exploration Research Project, Mineral Deposit Research Unit, University of British Columbia, Short Course Notes, 180 p.

Stanley, C.R., 2017, Lithogeochemical classification of igneous rocks using Streckeisen ternary diagrams: Geochemistry: Exploration, Environment, Analysis, 17, 63-91.

Stanley, C.R. and H.E. Madeisky, 1996, Lithogeochemical exploration for metasomatic zones associated with hydrothermal mineral deposits using molar element ratio analysis: Introduction, Lithogeochemical Exploration Research Project, Mineral Deposit Research Unit, University of British Columbia, Short Course Notes, 200 p.

Stanley, C.R. and J.K. Russell, 1989, Petrologic hypothesis testing with Pearce element ratio diagrams: Derivation of diagram axes: Contributions to Mineralogy and Petrology, 103, 78-89.

Stern, R. A., E.C. Syme, A.H. Bailes, and S.B. Lucas, 1995,

Paleoproterozoic (1.90-1.86) arc volcanism in the Flin Flon Belt, Trans-Hudson Orogen, Canada: Contributions to Mineralogy and Petrology, 119, 117-141.

Strang, G., 1993, Introduction to Linear Algebra: Wellesley-Cambridge Press.

Streckeisen, A.L., B.A. Zanettin, M.J. Le Bas, B. Bonin, P. Bateman, G. Bellini, A. Dude, S. Efremova, J. Keller, J. Lameyre, P.A. Sabine, R. Schmid, H. Sorensen, and A.R. Woodley, 2002, Igneous rocks; a classification and glossary of terms; recommendations of the International Union of Geological Science Subcommission on the Systematics of Igneous Rocks: Cambridge University Press.

Sun, S.S. and W.F. McDonough, 1989, Chemical and isotopic systematics of oceanic basalts: Implications for mantle composition and processes: Geological Society of London, Special Publications, 42, 313-345.

Syme, E.C., S.B. Lucas, A.H. Bailes, and R.A. Stern, 1998, Contrasting arc and MORB-like assemblages in the Paleoproterozoic Flin Flon Belt, Manitoba, and the role of intra-arc extension in localizing volcanic-hosted massive sulphide deposits: Canadian Journal of Earth Sciences, 36, 1767-1788.

Thompson, J.B., 1982, Composition space: An algebraic and geometric approach: Reviews in Mineralogy, 10, 1-31.

Urqueta, E., T.K. Kyser, A.H. Clark, C.R. Stanley, and C.J. Oates, 2009, Lithogeochemistry of the Collahuasi porphyry Cu-Mo and epithermal Cu-Ag (-Au) cluster, northern Chile: Pearce element ratio vectors to ore: Geochemistry: Exploration, Environment, Analysis, 9, 9-17.

Vance, R.K., 1989, Geochemistry and tectonic setting of the Early Proterozoic Yavapai Supergroup, Central Arizona: PhD Thesis, New Mexico Institute of Mining and Technology.

Vance, R.K. and K.C. Condie, 1987, Geochemistry of footwall alteration associated with the Early Proterozoic United Verde massive sulfide deposit, Jerome, Arizona: Economic Geology, 82, 571-586.

Vistelius, A.B. and O.V. Sarmanov, 1961, On the correlation between percentage values: major component correlation in ferromagnesian micas: Journal of Geology, 69, 145-153.

Winchester, J.A. and P.A. Floyd, 1977, Geochemical discrimination of different magma series and their differentiation products using immobile elements: Chemical Geology, 20, 325-343.

Wright, J.F. and C.H. Stockwell, 1934, West half of Amisk Lake area, Saskatchewan: Geological Survey of Canada, Summary Report 1933, Part C, 12-22.